Tropical Intraseasonal Oscillations in CFSv2 during Boreal Summer and Winter

Running Head: Intraseasonal Oscillations in CFSv2

V. Krishnamurthy

Center for Ocean-Land-Atmosphere Studies
George Mason University
Fairfax, Virginia

Revised
September 2016

Corresponding author:
V. Krishnamurthy
Center for Ocean-Land-Atmosphere Studies
Research Hall, MS 6C5
George Mason University
4400 University Drive

This is the author manuscript accepted for publication and has undergone full peer review but has not been through the copyediting, typesetting, pagination and proofreading process, which may lead to differences between this version and the Version of Record. Please cite this article as doi: 10.1002/joc.4948

Fairfax, VA 22030
E-mail: vkrishna@gmu.edu

Abstract

The simulation of the tropical intraseasonal oscillations (ISOs) by a coupled model in the Indo-Pacific region is examined in this study. The retrospective forecasts by the Climate Forecast System version 2 (CFSv2) of National Centers of Environmental Prediction for the period 1982–2010 have been analyzed and compared with observation. The leading Indian monsoon intraseasonal oscillation (MISO) during the boreal summer and the Madden-Julian Oscillation (MJO) during the boreal winter are extracted from daily precipitation anomalies in forecasts and observations by using a data-adaptive method. The model forecasts from May initial conditions simulates the observed spatial structure, magnitude and the northward and eastward propagation of MISO reasonably well. Similar performance is also evident in the simulation of the eastward propagating MJO in forecasts from November initial conditions. In the simulation of both the MISO and MJO by the model, the zonal wind at lower level shows appropriate observed relation with the precipitation and coupling with convection. The observed phase relations between precipitation and low-level relative vorticity and between precipitation and upper-level divergence in the zonal and meridional propagations are captured by the model. However, the variance of the ISOs differs from observation in certain regions, and the phase of the ISOs exhibits wide differences among the ensemble members of the forecast and with the observation. Comparison with the earlier model, CFS version 1, shows that the space-time structure and evolution of MISO and MJO are better simulated by CFSv2.

Keywords: Indian monsoon, Intraseasonal oscillation, MISO, MJO, CFSv2, Forecasts

1. Introduction

The tropical climate system in the Indo-Pacific region exhibits strong variability at intraseasonal time scale. The active-break cycle in the Indian monsoon during the boreal summer and the Madden-Julian Oscillation (MJO) during the boreal winter are major manifestations of the tropical intraseasonal variability (e.g., Krishnamurthy and Kinter, 2003; Zhang, 2005). In the Indian region, the active phase of the monsoon brings above-normal rainfall whereas the break phase leads to below-normal or no rainfall (Krishnamurthy and Shukla, 2000). The active (break) period coincides with the strengthening (weakening) of the mean monsoon circulation. The active phase starts with convective activity in the western equatorial Indian Ocean and propagates northward (Sikka and Gadgil, 1980) as well as eastward. The break phase is similar to the active phase but with the movement of suppressed convection zone. The intraseasonal variability of the Indian monsoon has been identified by several studies to occur in the range of 10–90 days (e.g., Yasunari, 1979; Lau and Chan, 1986). The active-break cycle actually consists of intraseasonal oscillations (ISOs) of different periods (Annamalai and Slingo, 2001; Krishnamurthy and Shukla, 2007). The leading monsoon ISO (MISO) has a broad-band spectrum centered at 45 days in convection (Annamalai and Sperber, 2005; Krishnamurthy and Shukla, 2008), rainfall (Krishnamurthy and Shukla, 2007), circulation (Krishnamurthy and Achuthavarier, 2012) and diabatic heating (Hazra and Krishnamurthy, 2015) with strong northward and eastward propagation. During the boreal winter, the MJO is stronger and consists of coupled convection and atmospheric circulation propagating eastward from the equatorial Indian Ocean to the Pacific Ocean (Madden and Julian, 1971, 1972, 1994; Zhang, 2005).

Although considerable progress has been made in modeling the tropical climate, the simulation and prediction of the tropical ISOs are still challenging (e.g., Kim *et al*., 2009; Sperber *et al*., 2013; Hung *et al*., 2013). The atmospheric general circulation models forced by observed sea surface temperature (SST) were found to produce ISOs which were less coherent with inadequate spatial extent and lacked proper eastward and northward propagation (Waliser *et al.*, 2003). The lack of variability over the oceanic region and the inaccurate phases of the simulated ISOs pointed to the importance of proper SST feedback (Kang *et al*., 2002). Based on controlled model experiments, Wang *et al*. (2005) suggested that coupled ocean-atmosphere models are necessary for better simulation of the monsoon rainfall. During the past decade, the usage of coupled models has become more common, and has led to organized assessment of coupled models. In the Coupled Model Intercomparison Project-3 (CMIP3), the MJO in most of the models had low variance and lacked coherent eastward propagation (Lin *et al*., 2006). However, the models from the later project CMIP5 showed improvement in MJO by generating larger variance and somewhat better spectral peak but were still unable to simulate realistic eastward propagation (Hung *et al*., 2013). The simulation of the life cycle of the boreal summer ISO over the monsoon region was found to be inadequate in CMIP3 models although the models showed eastward propagation (Sperber and Annamalai, 2008). Sperber *et al*. (2013) compared CMIP3 and CMIP5 models and found that the northward propagation was improved in several later models although major problems still exist in the simulation of the intraseasonal variability of the summer monsoon.

Coupled climate models are employed at major operational forecast centers for

subseasonal and seasonal predictions. The National Centers for Environmental Prediction (NCEP) has been providing seasonal forecasts with the Climate Forecast System version 1 (CFSv1) since 2004 (Saha *et al*., 2006) and with the upgraded CFS version 2 (CFSv2) since 2011 Saha *et al*., 2014). The CFSv2 includes improvements in the atmospheric and oceanic components of the model and in the data assimilation systems. The study by Wang *et al*. (2014) showed that the MJO prediction skill of CFSv2 has improved in comparison to CFSv1 while systematic errors are still present. The boreal summer MISO simulated by CFSv1 was found to have much longer period and less variance compared to observations but exhibited northeastward propagation (Achuthavarier and Krishnamurthy, 2011a). The SST variability and the ocean-atmosphere interaction in the Indian Ocean are important in properly simulating the propagation of MISO (Achuthavarier and Krishnamurthy, 2011b). Similarly, through experiments with CFSv1, Pegion and Kirtman (2008a, 2008b) concluded that the MJO during the boreal winter was better simulated when the air-sea interaction occurred through proper variation of SST at daily and intraseasonal time scales. The importance of air-sea interaction was also pointed out by other model studies in MISO (Fu *et al*., 2003) and MJO (Klingaman and Woolnough 2014).

The objective of this study is to investigate the performance of CFSv2 in simulating the leading tropical ISO during boreal summer and winter. The spatial structure, period and the propagation properties of the leading MISO and MJO simulated by CFSv2 will be analyzed to determine if any improvements have occurred compared to the simulations of CFSv1. The associated circulation features and possible mechanisms involving circulation will also be examined. For this purpose, the nine-month long retrospective forecasts of CFSv2 generated by

NCEP with a series of different initial conditions will be used. The MISO during the boreal summer and MJO during the boreal winter will be extracted in precipitation by using a suitable data-adaptive method. The spatial structure of MISO is known to extend into the Pacific in observations (Krishnamurthy and Shukla, 2008), and the eastward propagation of MJO into the Pacific is also well-known (Madden and Julian, 1994). Therefore, the domain used in this study will cover the entire tropical Indo-Pacific region.

The model and its forecasts, observed data and the method of analysis are described in section 2. In section 3, the mean climate and the extraction of the summer and winter ISOs will be described. Section 4 discusses the space-time evolution of the precipitation ISOs and the relation with circulation. Summary and conclusions are provided in section 5.

2. Model, data and method of analysis

2.1. Model and data

The CFSv2 is a globally coupled model currently used for operational seasonal forecasts by the NCEP. The atmospheric component is based on the NCEP Global Forecast System (GFS), and has 64 vertical levels and T126 horizontal resolution (nearly 100 km grid spacing). The ocean component is the Geophysical Fluid Dynamics Laboratory (GFDL) Modular Ocean Model version 4 (MOM4) with 40 vertical levels and 0.5° horizontal resolution which increases meridionally to 0.25° in the deep tropics. The CFSv2 includes Noah land model and GFDL Sea Ice Simulator. More details of CFSv2 and the modifications introduced are described by Saha *et*

al. (2010, 2014).

This study has used the nine-month retrospective forecasts generated by the NCEP. The forecasts are made from initial conditions of every fifth day starting from 1 January of every year during 1982–2010. On each initial day, an ensemble of four forecasts is generated from initial conditions of 0000, 0600, 1200 and 1800 UTC. In this study, the forecasts made from May and November initial conditions are used for analyzing, respectively, the boreal summer MISO and boreal winter MJO. The May forecasts in each year consist of an ensemble of 28 members starting from four initial conditions each on 1, 6, 11, 16, 21, 26 and 31 May during 1982–2010. In the November forecasts, an ensemble of 24 forecasts in each year is obtained from four initial conditions on 2, 7, 12, 17, 22 and 29 November of 1982–2010. The daily mean precipitation and horizontal winds at 850 and 200 hPa from the above forecasts are analyzed. The daily mean precipitation from Version 7 of Tropical Rainfall Measuring Mission (TRMM) 3B42 product on 0.25°×0.25° horizontal grid for the period 1998–2010 (Huffman *et al*., 2007) is used for observation. Although the TRMM data set does not cover the entire period of the forecasts, it has the advantage of including coverage over both and land and ocean. The horizontal wind data were obtained from the CFS Reanalysis (CFSR; Saha *et al*., 2010) for the period 1982–2010.

2.2. Method of analysis

The multi-channel singular spectrum analysis (MSSA; Ghil *et al*., 2002) is the method used in this study to extract the ISOs. This method is the multivariate version of the singular spectrum analysis introduced by Broomhead and King (1986). The MSSA has been successfully

used to extract the space-time structure of ISOs in previous studies of monsoon (e.g., Krishnamurthy and Shukla, 2008). Starting with a given time series of data at L grid points (or channels) and N discrete time intervals, a delayed co-ordinate approach is adopted by adding M lagged copies of the data. A grand lagged covariance matrix C is constructed and diagonalized to obtain LM eigenvalues and LM eigenvectors. Each eigenvector contains M lagged patterns and forms the space-time EOF (ST-EOF) while the corresponding space-time principal component (ST-PC) is of time length $N-M+1$. The eigenvalues explain the variance of the eigenmodes. The time series corresponding to each eigenmode is obtained as reconstructed component (RC) by multiplying the corresponding ST-EOF and ST-PC (see Ghil *et al*. 2002 for the formula). The RC is the data-adaptive filter which has the same spatial and time dimensions as the original time series. By adding all the RCs, the original time series is recovered. The eigenmodes obtained from MSSA can be oscillations, persistent modes or trends. A pair of consecutive eigenmodes with almost degenerate eigenvalues is oscillatory if the corresponding ST-PCs and ST-EOFs are in quadrature and have almost equal period (Plaut and Vautard, 1994; Ghil *et al*., 2002). The ISOs can be extracted by identifying such oscillations which emerge as a pair of eigenmodes. All the MSSA eigenmodes analyzed in this paper were found to be statistical significant at 5% level by following the Monte Carlo test against signals from red noise as discussed by Allen and Robertson (1996) and Allen and Smith (1996).

3. Mean and Intraseasonal oscillations in precipitation

As stated earlier, the boreal summer ISO in the Indo-Pacific region will be studied by

analyzing an ensemble of forecasts starting from 28 different initial conditions during May of each year for the period 1982–2010. The analysis will consider the forecasts up to 30 September of each year, spanning the summer monsoon season. For the boreal winter ISO, the ensemble of 24 forecasts starting from different initial conditions in November each year and ending in 31 March of the subsequent year for the period 1982–2010 will be used. A brief description of the mean and standard deviation of the precipitation is useful before discussing the ISOs. The forecasts from May and November initial conditions will be referred to as May and November forecasts for brevity, hereafter. Although retrospective forecasts have been used, the focus of this study is not to test the accuracy of the day-to-day forecasts compared to observations but to examine whether the model has simulated the features of ISOs by examining the statistics of the retrospective forecasts.

3.1. Mean and standard deviation

The climatological mean of precipitation for the June–September (JJAS) season in observation (TRMM) and May forecasts is shown in Fig. 1. The climatology in the observation is the average of 1998–2010 (Fig. 1a) while it is the average over all ensemble members and over the period 1982–2010 in the forecasts (Fig. 1b). The mean rainfall in the observation has large values over the west coast and central part of India, the Bay of Bengal and the Intertropical Convergence Zone (ITCZ) in the Pacific (Fig. 1a). The model has reproduced the observed spatial structure reasonably well in the Indian monsoon region and the Pacific (Fig. 1b). The difference map between the model and observation (Fig. 1c) indicates that the model has deficit

rainfall over parts of India and the Maritime Continent but higher values, by up to 4 mm day^{-1}, in the Indian Ocean and the ITCZ in the Pacific. The standard deviation of the daily anomalies of precipitation for JJAS season for observation (TRMM) and May forecasts are plotted in Figs. 1d and 1e, respectively. The standard deviation of the forecasts is calculated by stringing together all the ensemble members (and not of the ensemble mean) for 1982–2010. The spatial structure of the standard deviation in the observation (Fig. 1d) is similar to that of the climatological mean (Fig. 1a). Although the spatial structure of the standard deviation in the forecasts resembles that of the observation, the difference map between the forecasts and observation (figure not shown) indicates that the model underestimates over parts of India, the Maritime Continent, and warm pool and equatorial regions of the Pacific and overestimates over the northern part of the tropical Pacific.

The climatological mean and the daily standard deviation of the precipitation for the boreal winter are also presented in Fig. 1. The climatology and the standard deviation of the December–March (DJFM) season are calculated for observation (TRMM) and November forecasts in the same manner as in the case of the boreal summer. The larger values in the DJFM climatology of the observation (Fig. 1f) occur in the Southern Indian Ocean, the Maritime Continent, the ITCZ and the South Pacific Convergence Zone (SPCZ). The model is again able to reproduce the observed structure fairly well (Fig. 1g). The difference map between the model and observation (Fig. 1h) indicates that the forecasts have higher values in the southern Indian Ocean and the SPCZ and lower values over the Maritime Continent and Australia. Generally, both during summer and winter, the model produces more mean rainfall over the oceanic region

and less over the land regions compared to observation. The standard deviation of the DJFM season in the observation (Fig. 1i) has a spatial structure similar to that of the mean (Fig. 1f). The model (Fig. 1j) captures the observed structure of the standard deviation to a large extent. The difference map between the model and observation (figure not shown) indicates that the standard deviation is lower over the Maritime Continent, ITCZ and Australia and higher over the Southern Indian Ocean and the SPCZ. The model produces more (less) daily activity where the mean is higher (lower) compared to observation both during summer and winter.

3.2. Active-break cycle

The intraseasonal variability in the summer monsoon is manifested through active phases when there is high rainfall and break phases with weak or no rainfall over the Indian region. The intraseasonal variability in the model forecasts is examined by constructing composites of daily precipitation anomalies based on active and break periods over India during JJAS. For this purpose, the extended Indian monsoon rainfall (EIMR) index (Goswami *et al*. 1999), defined as the rainfall averaged over (70°E–110°E, 10°N–30°N), is used. The EIMR index corresponds to a region of intense monsoon activity (Fig. 1a and 1d). The selection of active (break) period is based on the criterion that the daily EIMR index is above (below) a threshold of one-half the standard deviation of the daily EIMR index for at least five consecutive days. This criterion is the similar to that used by Krishnamurthy and Shukla (2008).

The active and break composites in the observation were computed using TRMM precipitation for JJAS of 1998–2010. The model composites were first constructed for each

ensemble member of the May forecasts by identifying the active and break periods from that ensemble member's daily EIMR index for JJAS of 1982–2010, and then the ensemble mean of the composites was computed. The difference between the active and break composites of the daily precipitation anomalies is shown in Fig. 2. The observation composite (Fig. 2a) shows positive anomalies along the west coast and over the central part of India and the Bay of Bengal while negative anomalies are found in the equatorial Indian Ocean and the West Pacific. The north-south dipole structure between 65°E–100°E is an important feature of the active-break cycle and represents a particular phase of northward propagation of the convective activity. The active-break composite of the model forecasts (Fig. 2b) has good correspondence with the observational composite (Fig. 2a) both in the spatial structure and magnitude and captures the dipole structure and the tilted structure of positive anomalies extending from India to the West Pacific. When the composite of the model forecasts is based on the active and break phases of the observation (Fig. 2c), it shows a complete absence of the dipole structure and almost no rainfall activity over the Indian region and the West Pacific. The reason for this difference is that the phase of the daily variability the EIMR index is different in each ensemble member at any given time and different from the phase of the observation's EIMR index.

A similar analysis was performed for the boreal winter with the November forecasts. For identifying the active and break cycles in the winter, an index of precipitation averaged over (110°E–150°E, 20°S–0°) is used. This index also corresponds to a region of high rainfall activity in both the mean and standard deviation (Figs. 1f and 1i), and will be referred to as the Maritime Continent-Australia monsoon rainfall (MAMR) index. The active minus break composites were

constructed with daily precipitation anomalies of observation (TRMM) and November forecasts for DJFM season using MAMR index, in exactly the same manner as in the boreal summer case. The observation composite (Fig. 2d) has positive anomalies over Maritime Continent and northern Australia and weaker negative anomalies to the east and west. This structure represents a particular phase of the eastward propagation of the MJO. The model composite based on the MAMR index of the forecasts (Fig. 2e) shows a good simulation of the observation pattern (Fig. 2d) both in structure and magnitude. However, the model composite based on the MAMR index of observation (Fig. 2f) is not a good representation of the observed pattern although it is able to capture the anomalies of proper sign in its spatial structure, and seems to be slightly better than the summer composite.

3.3. Leading intraseasonal oscillation

The active-break cycle consists of intraseasonal oscillations with different periods. Observational studies of the boreal summer monsoon have indicated that the leading mode of intraseasonal variability is a nonlinear oscillation with a period of 45 days (Krishnamurthy and Shukla 2007, 2008). The MJO is also an oscillation of similar period dominant during the boreal winter (Madden and Julian, 1971, 1972). In view of the results of the previous subsection, it is of interest to investigate the leading mode of intraseasonal variability in the daily forecasts of the model. For this purpose, the daily precipitation anomalies of the observation and forecasts are decomposed by applying MSSA, similar to the method used by Krishnamurthy and Shukla (2007, 2008). Since this study is assessing both MISO and MJO, the spatial domain is selected to

be the entire tropical Indo-Pacific region. The MSSA is applied on daily precipitation anomalies over the domain (40°E–80°W, 35°S–35°N). For the boreal summer, the MSSA was applied on daily anomalies for the period of May to September. The May forecasts consist of 28 ensemble members, each starting with a different initial condition in May. The MSSA was applied separately on each ensemble member for the period 1982–2010. In the case of boreal winter, the MSSA was applied on daily anomalies for the period of November to March, separately for each of the 24 ensemble members of the November forecasts. Similarly, the MSSA was applied on the TRMM observation separately for the boreal summer and winter. A lag window of 61 days at one-day interval was used in all the MSSA. The ST-EOF and ST-PC of each MSSA eigenmode of the ensemble members and observation were found. Using these, the RCs of each eigenmode, which are the MSSA-decomposed components of the total anomalies, were computed.

For each ensemble member in the model forecasts and for observation, the leading oscillation was identified. An oscillation occurs as a pair of consecutive eigenmodes with almost degenerate eigenvalues and with ST-PCs in quadrature. These and other criteria set forth by Plaut and Vautard (1994) were used for the identification of the leading nonlinear oscillation. Further statistical analysis is performed on the RC of the leading ISO identified in each case. A spatial EOF analysis was carried out on the ISO RC of each ensemble member in the models and in the observation, and the power spectrum of the first PC of each RC was obtained. The power spectra are plotted for the summer and winter in Fig. 3a and 3b, respectively. All the spectra are broad band, reflecting the nonlinear character of the ISOs. The central period of the spectrum in the observation for boreal summer MISO is 45 days whereas it ranges from 47 to 70 days with an

average period of 61 days in May forecasts (Fig. 3a). In the boreal winter MJO, the spectrum in the observation has a central period of 54 days while the November forecasts have spectra with period ranging from 60 to 72 days with an average period of 67 days (Fig. 3b). Figure 3 reveals that the model spectra are slightly further apart from the observational spectra and broader in boreal summer compared to the spectra of boreal winter. It is of interest to note that the period of MJO is slightly higher than that of MISO in observation. The leading ISO in the Indian monsoon region during the boreal summer in CFSv1 was found to have a broad-band spectrum centered at 106 days (Achuthavarier and Krishnamurthy, 2011a). The study by Achuthavarier and Krishnamurthy (2011a) was based on a long simulation whereas the present study is based on retrospective forecasts. The comparison is still reasonable since it is the statistics of the ISOs that has been analyzed and because of the ergodic nature of the solutions of dynamical systems such as the model. Therefore, the MISO in CFSv2 seems to have a better representation of the observed period compared to CFSv1. An examination of the power spectra of the EIMR index of the total precipitation anomaly (figure not shown) indicated that the model forecasts are able to capture the observed variation of power with period at all subseasonal time scales.

The standard deviation of the daily RC of the boreal summer MISO is plotted in Figs. 3c and 3e for observation and May forecasts, respectively. The observation (Fig. 3c) has large values in west coast, Bay of Bengal, eastern Indian Ocean and West Pacific while the signal extends up to the west coast of North America. The model's pattern (Fig. 3e) has good resemblance to the observed pattern (Fig. 3c). However, the model's standard deviation is lower over India, Maritime Continent and western equatorial Pacific and higher over parts of Indian

and Pacific oceans as revealed by the difference map (Fig. 3g). The standard deviation of the daily RC of the boreal winter MJO in observation and November forecasts are shown in Figs. 3d and 3f, respectively. Large values are seen around the Maritime Continent and in the SPCZ in the observation (Fig. 3d). The forecasts show a band of large values extending from the Central Indian Ocean to the SPCZ (Fig. 3f). The difference map in Fig. 3h shows that the model overestimates over a large area in the Pacific and a smaller region in the Indian Ocean while showing lesser values in Bay of Bengal, Maritime Continent and Australia. For both observation and forecasts, the standard deviation of the ISOs is about 10–20% (varying spatially) of the corresponding standard deviation of the total mean precipitation shown in Fig. 1 (figures of the ratio not shown).

4. Space-time structures of the ISOs

The space-time structure of the ISO can be understood with the help of phase composites. The amplitude $A(t)$ and phase $\phi(t)$ of the ISO, as a function of time t, are determined by following the method suggested by Moron *et al*. (1998). The space-time evolution of the ISO during an averaged cycle of the oscillation, with ϕ varying from 0 to 2π, is described by constructing the phase composites of the RC. Considering eight phase intervals, such that $(k-1)\pi/4 \le \phi \le k\pi/4$ where $k = 1, 2, \ldots, 8$, the RC is averaged over all ϕ in each phase interval k over the entire time length of the RC to obtain the phase composites.

4.1. Boreal summer MISO

The phase composites of the precipitation RC of the boreal summer MISO for phase intervals 1 through 4 are shown in Figs. 4a and 4b, respectively, for observation and May forecasts. In the case of the model, the phase composite is the average of all the ensemble members. The phase composites cover May–September of all years. In phase 1 of the phase composite of the observation (Fig. 4a), positive anomalies of precipitation are present over a large area from the Arabian Sea to the West Pacific in a tilted pattern while negative anomalies are present to north over the foothills of the Himalayas and the West Pacific. A weak band of negative anomalies extends along the ITCZ up to the west coast of North America in the Pacific. The band of positive anomalies moves northward in phases 2 and 3, resulting in the establishment of the active phase over India. At the same time, negative anomalies appear in the equatorial Indian Ocean in phase 2 and expand and propagate eastward in phase 3 while the negative anomalies from the previous cycle grow along the west coast of North America. In phase 4, the negative anomalies further expand and move northward over the Indian peninsula and the Bay of Bengal and the positive anomalies move further northeastward over the Pacific. Since the phase composites are averages over many cycles of MISO, the composites in phases 5–8 (figure not shown) are almost mirror images of phases 1–4, respectively, with anomalies of opposite sign. During phases 6–7, the break phase is established over India.

The phase composites of the MISO simulated by the model's May forecasts (Fig. 4b) show good correspondence with the composites of observation (Fig. 4a) in spatial structure, magnitude and propagation. The tilted structure of the positive anomalies, which results from northward propagation starting at different times because of eastward propagation along the

equatorial region, is well simulated by the model in both the spatial extent and the magnitude. The genesis of the negative anomalies and the subsequent expansion and propagation in the Indian Ocean are also captured by the model. The model forecasts also show northward propagation in the West Pacific. Yet, there are some differences between the model and observation. The band of anomalies along the Pacific ITCZ is very weak although the model is able to generate the signal along the west coast of North America. The anomalies in the forecasts are weaker over India and do not propagate as north as they do in the observation. This is consistent with the model's deficit in the standard deviation over India (Fig. 3g). The leading ISO in CFSv1, which had a longer period at 106 days, exhibited northward and eastward propagation over the Indian region but not over the Maritime Continent and West Pacific (Achuthavarier and Krishnamurthy 2011a). The magnitude of this ISO was considerably less over most of the region. Another ISO in CFSv1, with a period of 57 days, showed poor propagation properties over the entire region. The MISO in CFSv2 seems to simulate the spatial structure, magnitude and propagation better than the ISOs in CFSv1.

The eastward and northward propagations are important features of MISO, which can be further examined through Hovmöller diagrams. For this purpose, the phase composites of MISO RC were constructed at phase intervals of length *À*/12. The eastward propagation mainly takes place over the equatorial region. Therefore, the phase composite of the RC, averaged over 10°S–10°N, is shown as longitude-phase diagram in Figs. 5a and 5b, respectively, for observation and May forecasts. In the observation, there is an eastward propagation to the east of 60°E (Fig. 5a). This eastward propagation is clearly seen in the phase composites of the forecasts also (Fig. 5b)

but does not extend as far east as in the observation. The forecast anomalies are weaker over the Maritime Continent and the West Pacific. The northward propagation over the monsoon region is determined by averaging the MISO RC over 60°E–95°E and plotting it as latitude-phase diagram, as shown in Figs. 5c and 5d, respectively, for observation and forecasts. The observation shows southward propagation to the south of the equator and northward propagation to the north of the equator (Fig. 5c). The model also shows northward propagation from the equator but ends at 21°N which is about 2–3° short of observation (Fig. 5d). The southward propagation to the south of the equator is not as pronounced as in the observation.

4.2. Boreal winter MJO

The phase composites of the precipitation RC for the first half cycle of the boreal winter MJO for are shown in Figs. 6a and 6b for observation and November forecasts, respectively. The phase composite in the model is the average of all the ensemble members. The phase composites cover the period of November–March each year. In the observation (Fig. 6a), strong negative anomalies are present around a part of the Maritime Continent and the northern coast of Australia along with weak positive anomalies in the Indian Ocean and Central Pacific in phase 1. The negative anomalies move eastward into the SPCZ, forming a tilted pattern during phases 2–4. The positive anomalies intensify and also propagate eastward in the region south of the equator from phase 2 to 4. At the same time, a thin band of positive anomalies appear along the ITCZ in the Pacific, slightly north of the equator. However, there is no signal at the coast of North America as in the case of MISO during the boreal summer.

In the model's November forecasts, the phase composites of the MJO (Fig. 6b) reproduce the spatial structure, magnitude and propagation of the observed composites (Fig. 6a) fairly well. The eastward propagation of the negative anomalies from the Maritime Continent to the central Pacific is also simulated by the model, including the tilted structure in the SPCZ. The magnitude of these anomalies is slightly higher compared to observation, consistent with the model's excess standard deviation over the Pacific (Fig. 3h). Positive anomalies are generated in the Indian Ocean in phase 1 and expand in phase 2 but with lesser magnitude. In phases 3–4, the positive anomalies move eastward but with slightly higher magnitude compared to observation. However, the positive anomalies also expand westward in the Indian Ocean, unlike in the observation. The model shows the observed thin band of positive anomalies in the ITCZ over the Pacific. The assessment of CFSv1 by Pegion and Kirtman (2008b) showed that the boreal winter MJO simulated by CFSv1 had less spatial extent compared to observation and was not well organized over the Indian Ocean. The period of the MJO was also much longer, similar to MISO, in CFSv1 with slower propagation and stalling over the Maritime Continent. The space-time structure of the winter MJO in CFSv2 seems to show improved spatial coverage and propagation properties.

The propagation properties of the MJO in both the observation and model forecasts can be further studied with Hovmöller diagrams using the RCs constructed at phase interval of length *À*/12. The longitude-phase cross-section of the RC averaged over 10°S–10°N reveals clear eastward propagation in observation (Fig. 7a) and November forecasts (Fig. 7b). The latitude-phase cross-section of the MJO RC, averaged over 90°E–120°E, suggests southward propagation to the south of the equator in observation (Fig. 7c) but not in the model forecasts (Fig. 7d).

However, there is northward propagation of weaker anomalies between equator and 10°N in both observation and model. The lack of strong southward propagation to the south of the equator in the MJO is a big difference with the MISO which showed strong northward propagation.

4.3. Simulation of phases

The phase composites of the model forecasts, discussed previously, have fairly good correspondence with the observed composites. The composites were computed on the basis of phase intervals varying from 0 to 2$\grave{A}$ for each oscillation. Here, the phases of the model ISOs are compared with those of the observation in actual time. The EIMR index of the MISO RC from observation and May forecasts is plotted in Figs. 8a for the period May–September 2001, as an example. The nonlinear oscillatory behavior is clearly evident in both observation and forecasts. Although the amplitude of the model's MISO is comparable to that of the observation, the phase varies with considerable difference among the ensemble members of the forecast and between forecast and observation. While some of the ensemble members of the forecasts stay somewhat closer to the observation for some time, others differ considerably from the beginning of the forecast period. All the forecasts are out of phase by about the middle of July.

The model forecast seems to be better when the initial amplitude and initial phase of the model ISO are closer to those of the ISO in observation (Fig. 8b). Two forecasts starting on 6 May (6 hours apart) stay close to the observed MISO until the middle of July, implying a considerably high predictability. The two forecasts, while staying close to each other, diverge from the observation and become out of phase by the middle of August. Two other forecasts,

initiated on 16 May (6 hours apart), are out of phase with the observation right from the beginning and throughout the entire period. The two forecasts, however, stay close to each other.

Similar behavior is also seen in the MJO during the boreal winter. The MAMR index of the MJO is shown in Fig. 8c for observation and November forecasts for the period Nov 2001 – March 2002. The amplitude of the forecast MJO is comparable to that of the observation. In this case also, the phase of the forecast MJO displays considerable variability among the ensemble members. Several ensemble members of the forecast stay closer to the observation until the beginning of January. Almost all the forecasts are out of phase beyond the middle of January. In the winter MJO forecasts (Fig. 8c), more ensemble members seem to evolve closer to the observation for about two months compared to the summer MISO forecasts (Fig. 8a).

4.4. Relation with circulation

The features of circulation associated with MISO and MJO are now studied. Some possible mechanisms involving circulation for the propagation of the ISOs are also examined. In both the boreal summer and winter ISOs, there is a strong coupling between the zonal circulation and convection. The relation of the precipitation ISOs with the circulation is examined with the help of phase composites of zonal wind using the CFSR data for observation and model forecasts. The phase composites of 850 hPa zonal wind anomalies for the first half cycle of the boreal summer MISO are shown in Figs. 9a and 9b for observation and May forecasts, respectively. The wind composites were constructed using the same phases as in the precipitation composites (section 4.1). The period covers May–September each year, and total anomalies of

the zonal wind are used. Positive anomalies appear in the equatorial India Ocean in phase 1, and then strengthen, expand in zonal direction and move northward into the Indian subcontinent during phases 2–4 in the observation (Fig. 9a). Negative anomalies accompany to the north and south of the positive anomalies. These correspond to the anti-cyclonic flow over India and cyclonic flow in the Indian Ocean. The northward propagation of the zonal wind is consistent with the precipitation composites (Fig. 4a) and with the MISO of circulation discussed by Krishnamurthy and Achuthavarier (2012). The Pacific is mostly covered by easterlies except for westerlies near the west coast of North America and South America in phase 1. The spatial structure, magnitude and the northward propagation of MISO in the model forecasts (Fig. 9b) have good correspondence with the observation (Fig. 9a) in all the four phase intervals. However, the zonal wind is considerably weaker over most of the central and eastern Pacific.

The phase composites of 850 hPa zonal wind for the boreal winter MJO are presented in Figs. 10a and 10b for observation and November forecasts, respectively. The period covered is November–March of each year. In the observation (Fig. 10a), easterlies propagate from the equatorial Indian Ocean to the Pacific Ocean during phases 1–4, followed by westerlies in the Indian Ocean. Corresponding to the precipitation zones (Fig. 6a), the westerlies and easterlies are present to the west and east of the positive anomalies of precipitation, respectively, in each phase. This is consistent with the known evolution of the convection-circulation coupling (e.g., Sperber 2003; Zhang 2005). The composites of the model forecasts (Fig. 10b) also reveal easterlies propagating eastward, followed by westerlies, along the equatorial Indian and Pacific Oceans during phases 1–4, similar to the evolution in observation (Fig. 10a). The westerlies are

weaker in phase 2 while the easterlies are weaker over the northern part of the Pacific in the model compared to observation.

To show that convectively coupled process is involved in the model's ISOs, the phase composites of the outgoing longwave radiation (OLR), which represents deep convection, are constructed. The phase composites of OLR for the first half cycle of MISO (boreal summer) and MJO (boreal winter) in the model forecasts are plotted in Figs. 11a and 11b, respectively. The amplitude, structure and propagation of the OLR have good correspondence with those of precipitation in both MISO (Figs. 11a and 4b) and MJO (Figs. 11b and 6b). The coupling between convection and circulation is revealed when compared with the composites of low-level zonal wind (Figs. 9b and 10b). In MISO, the anti-cyclonic (cyclonic) flow (Fig. 9b) is accompanied by enhanced (suppressed) convection (Fig. 11a). The eastward propagating convection zones in MJO (Fig. 11b) are accompanied by westerlies to the west and easterlies to the east (Fig. 10b). Thus, the model forecasts capture the observed convectively coupled circulation during summer and winter.

A simple mechanism for the meridional propagation of convection involves low-level cyclonic vorticity and moisture convergence to the north of the convection zone (e.g., Goswami, 2005). To examine this mechanism and to find further relation with circulation, the phase composites of 850 hPa relative vorticity and 200 hPa divergence are studied through Hovmöller diagrams. The longitude-phase cross section of 850 hPa vorticity averaged over 10°S–10°N in MISO is shown in Figs. 12a and 12b for observation and May forecasts, respectively. The corresponding composites of the precipitation RC are also shown. The positive (negative)

vorticity is ahead to the east of the precipitation (dry) zones during the eastward propagation both in the observation and model forecasts. However, the vorticity is weaker in the model and does not extend as far east as in the observation. The latitude-phase cross-sections of 850 hPa vorticity and the precipitation RC averaged over 60°E–95°E are plotted in Figs. 12c and 12d for observation and forecasts, respectively. In the observation (Fig. 12c), the precipitation (dry) zone is led by cyclonic (anticyclonic) vorticity to the north of the equator during the northward propagation. A similar phase relation between vorticity and precipitation is evident in the forecasts also (Fig. 12d). A consistent phase relation between vorticity and precipitation is also seen to the south of the equator in both observation and forecasts.

The phase composites of 200 hPa divergence and the corresponding precipitation RC are shown in Fig. 13 for MISO. The longitude-phase cross section averaged over 10°S–10°N (Fig. 13a) in observation shows that precipitation (dry) regions are co-located with the upper level divergence (convergence), indicating deep convection process. Similar relation between the upper level divergence and precipitation is also evident in the May forecasts (Fig. 13b), although with less intensity. The divergence in the model does not extend as far eastward as in the observation. The latitude-phase cross sections averaged over 60°E–95°E show more intense divergence (convergence) at upper level co-located with the precipitation (dry) zone and propagating north both in observation (Fig. 13c) and May forecasts (Fig. 13d).

For the MJO during DJFM, the longitude-phase cross section of the phase composites of 850 hPa relative vorticity and the precipitation RC averaged over 10°S–10°N are plotted in Figs. 14a and 14b for observation and November forecasts, respectively. In the observation, positive

(negative) vorticity leads the precipitation with pronounced eastward propagation (Fig. 14a). This phase relation between vorticity and precipitation is well captured by the forecasts (Fig. 14b). The latitude-phase cross section averaged over 90°E–120°E of vorticity shows weaker southward propagation to the south of the equator in the observation (Fig. 14c). The precipitation (dry) zone is led by cyclonic (anticyclonic) vorticity. The model forecasts also reproduce the weak southward propagation and the observed phase relation with the precipitation (Fig. 14d).

The phase composites of 200 hPa divergence and the precipitation RC for the MJO are shown in Fig. 15. The divergence and precipitation are co-located in MJO also and show strong eastward propagation in the longitude-phase cross section averaged over 10°S–10°N in the observation (Fig. 15a). The November forecasts also reveal the in-phase relation between divergence and precipitation along with eastward propagation (Fig. 15b). The latitude-phase cross-section averaged over 90°E–120°E also shows the in-phase relation between divergence and precipitation both in observation (Fig. 15c) and forecasts (Fig. 15d). However, the divergence does not reveal even weaker southward propagation.

5. Summary and discussion

In the tropical regions, the prediction of climate variability at intraseasonal time scale is important because of the impact of ISOs and challenging because of the complexity of the problem. Predictions beyond the weather time scale and up to a season are now part of operational forecasting centers. The NCEP has been carrying out seasonal predictions since 2004 using CFSv1 and by its successor CFSv2 since 2011. The present study has analyzed the

simulation of the tropical ISOs by CFSv2 during boreal summer and winter. The retrospective forecasts prepared by the NCEP for the period 1982–2010 were examined to determine the model's ability to simulate the summer MISO and winter MJO. Comparison with the observations and the ISOs simulated by CFSv1 was also carried out. The CFSv2 was found to simulate the spatial structure, period and propagation of MISO and MJO with reasonably good correspondence with the observation and showed improvement over CFSv1.

The leading ISOs were extracted from the daily precipitation anomalies of the ensemble of forecasts and observation by using MSSA. This data-adaptive method did not require any pre-assumption on the time scale of the extracted eigenmodes. The ensemble members of the forecasts are able to exhibit nonlinear oscillations which emerged as leading ISOs. The May forecasts of the model simulate the spatial structure and evolution of the summer MISO with good resemblance to the observation. The model's MISO also reproduces observed northward and eastward propagation over the Indo-Pacific region. The model falls slightly short in its northward propagation over India. The variance of MISO is comparable to observation over most of Indo-Pacific region except for deficit over India and the Maritime Continent. The peak period of the MISO in the model's ensemble members ranges from 47 to 70 days with an average period of 61 days which is higher than the observed period of 45 days. This discrepancy is also reflected through the ensemble spread in the phase of the MISO compared to observation. The model also showed the observed relation with the lower level zonal wind in spatial structure and propagation except for weaker magnitude over the Pacific. The model also revealed the coupling between circulation and convection in MISO. The observed phase relations of precipitation with

low-level relative vorticity and upper-level divergence involved in the zonal and meridional propagations were reproduced by the forecasts.

The boreal winter MJO in the November forecasts of the model is also reasonably well simulated in comparison to observation. The peak period of the ensemble members of the forecast is in the range 60–72 days with an average period of 67 days, higher than the observed period of 54 days. Although the spatial structure of the variance of the forecast MJO is similar to the observation, the variance is higher in the model over the SPCZ and less over the Maritime Continent. The simulation of the space-time evolution of the winter MJO by the model forecasts is comparable to the observation. The model reproduces the eastward propagation of the MJO signal with appropriate magnitude and spatial structure. However, the anomalies are more extended over the Indian Ocean. The westerlies and easterlies relative to the precipitation zone are also well simulated by the model in the lower level although with lesser magnitude over certain parts of the Pacific. The convectively coupled circulation was also evident in the model's MJO. The observed phase relation between precipitation and low-level vorticity and between precipitation and upper-level divergence were also captured by the model.

There is no discernable difference in the model's ability to simulate the boreal summer MISO and winter MJO. Although many features of the ISOs are reasonably well simulated by the model, there is a considerable ensemble spread in the phase of the model ISOs compared to observation. However, if the initial phase and the amplitude of the model ISO are closer to those of the observed ISO, the forecast ISO evolves close to the observed ISO for about two months, showing higher predictability. Compared with the CFSv1 simulations analyzed by earlier studies

(Pegion and Kirtman 2008a, 2009b; Achuthavarier and Krishnamurthy 2011a, 2011b), CFSv2 seems to have improved the simulation of both summer MISO and winter MJO in period, spatial structure and propagation. The reasons for the improvement in CFSv2 need further investigation. The earlier studies on CFSv1 pointed out the important role of air-sea interaction, especially over the Indian Ocean, in both the ISOs. It is of interest to determine if the air-sea interaction and heat budget are better over the Indian Ocean in CFSv2. Mechanistic experiments with regional decoupling separately over the Indian and Pacific Oceans using CFSv2 will be helpful.

Acknowledgments

This work was supported by National Science Foundation (grant ATM-0830068), National Oceanic and Atmospheric Administration (grant NA09OAR4310058), and National Aeronautics and Space Administration (grant NNX09AN50G). The author thanks NCEP for reforecasts of CFSv2.

References

Achuthavarier D, Krishnamurthy V. 2011a. Daily modes of South Asian summer monsoon variability in the NCEP Climate Forecast System. *Clim. Dyn.* **36**: 1941–1958.

Achuthavarier D, Krishnamurthy V. 2011b. Role of Indian and Pacific SST in Indian summer monsoon intraseasonal variability. *J. Clim.* **24**: 2915–2930.

Allen MR, Robertson AW. 1996. Distinguishing modulated oscillations from coloured noise in multivariate datasets. *Clim. Dyn.* **12**: 775–784.

Allen MR, Smith LA. 1996. Monte Carlo SSA: Detecting irregular oscillations in the presence of colored noise. *J. Clim.* **9**: 3373–3404.

Annamalai H, Slingo HM. 2001. Active/break cycles: diagnosis of the intraseasonal variability of the Asian summer monsoon. *Clim. Dyn.* **18**: 85–102.

Annamalai H, Sperber KR. 2005. Regional heat sources and the active and break phases of boreal summer intraseasonal (30-50 day) variability. *J. Atmos. Sci.* **62**: 2726–2748.

Broomhead DS, King GP. 1986. Extracting qualitative dynamics from experimental data. *Physica D* **20**: 217–236.

Fu X, Wang B, Li T, McCreary JP. 2003. Coupling between northward-propagating, intreaseasonal oscillations and sea surface temperature in the Indian Ocean. *J. Atmos. Sci.* **60**: 1733–1753.

Ghil M, Allen MR, Dettinger MD, Ide K, Kondrashov D, Mann ME, Robertson AW, Saunders A, Tian Y, Varadi F, Yiou P. 2002. Advanced spectral methods for climatic time series. *Rev. Geophys.* **40(1)**: 1003, doi:10.1029/2000RG000092.

Goswami BN. 2005. South Asian monsoon. In *Intraseasonal variability in the atmosphere-ocean climate system*, Lau WKM, Waliser DE (eds). Praxis: Chichester, 19–61.

Goswami BN, Krishnamurthy V, Annamalai H. 1999. A broad-scale circulation index for the interannual variability of the Indian summer monsoon. *Q. J. R. Meteorol. Soc.* **125**: 611–633.

Hazra A, Krishnamurthy V. 2015. Space-time structure of diabatic heating in monsoon intraseasonal oscillation. *J. Clim.* **28**: 2234-2255.

Huffman GJ, Adler RF, Bolvin DT, Gu G, Nelkin EJ, Bowman KP, Hong Y, Stocker EF, Wolff DB. 2007. The TRMM Multisatellite Precipitation Analysis (TMPA): Quasi-global, multi-year, combined-sensor precipitation estimates at fine scales. *J. Hydrometeorol.* **8**: 38–55.

Hung M-P, Lin J-L, Wang W, Kim D, Shinoda T, Weaver SJ. 2013. MJO and convectively coupled equatorial waves simulated by CMIP5 climate models. *J. Clim.* **26**: 6185–6214.

Kang I-S, Jin K, Wang B, Lau K-M, Shukla J, Krishnamurthy V, Schubert SD, Waliser DE, Stern WF, Kitoh A, Meehl GA, Kanamitsu M, Galin VY, Satyan V, Park C-K, Liu Y. 2002. Intercomparison of the climatological variations of Asian summer monsoon precipitation simulated by 10 GCMs. *Clim. Dyn.* **19**: 383–395.

Kim D, Sperber K, Stern W, Waliser D, Kang I-S, Maloney E, Wang W, Weickmann K, Benedict J, Khairoutdinov M, Lee M-I, Neale R, Suarez M, Thayer-Calder K, Zhang G. 2009. Application of MJO simulation diagnostics to climate models. *J. Clim.* **22**: 6413–6436.

Klingaman NP, Woolnough SJ. 2014. The role of air-sea coupling in the simulation of the Madden-Julian oscillation in the Hadley Centre model. *Q. J. R. Meteorol. Soc.* **140**: 2272–2286.

Krishnamurthy V, Achuthavarier D. 2012. Intraseasonal oscillations of the monsoon circulation over South Asia. *Clim. Dyn.* **38**: 2335–2353.

Krishnamurthy V, Kinter JL III. 2003. The Indian monsoon and its relation to global climate variability. In *Global climate*, Rodó X, Comín FA (eds). Springer: Berlin, 186–236.

Krishnamurthy V, Shukla J. 2000. Intraseasonal and interannual variability of rainfall over India. *J. Clim.* **13**: 4366–4377.

Krishnamurthy V, Shukla J. 2007. Intraseasonal and seasonally persisting patterns of Indian monsoon rainfall. *J. Clim*. **20**: 3–20.

Krishnamurthy V, Shukla J. 2008. Seasonal persistence and propagation of intraseasonal patterns over the Indian monsoon region. *Clim. Dyn.* **30**: 353–369.

Lau K-M, Chan PH. 1986. Aspects of the 40–50 day oscillation during the northern summer as inferred from outgoing longwave radiation. *Mon. Wea. Rev.* **114**: 1354–1367.

Lin J-L, Kiladis GN, Mapes BE, Weickmann KM, Sperber KR, Lin W, Wheeler MC, Schubert SD, Del Genio A, Donner LJ, Emori S, Gueremy J-F, Hourdin F, Rasch P, Roeckner E, Scinocca JF. 2006. Tropical intraseasonal variability in 14 IPCC AR4 climate models. Part I: Convective signals. *J. Clim.* **19**: 2665–2690.

Madden RA, Julian PR. 1971. Description of a 40–50 day oscillation in the zonal wind in the tropical Pacific. *J. Atmos. Sci.* **28**: 702–708.

Madden RA, Julian PR. 1972. Description of global-scale circulation cells in the tropics with a 40–50 day period. *J. Atmos. Sci.* **29**: 1109–1123.

Madden RA, Julian PR. 1994. Observations of the 40-50 day tropical oscillation – A review. *Mon. Wea. Rev.* **122**: 814–837.

Moron V, Vautard R, Ghil M. 1998. Trends, interdecadal and interannual oscillations in global sea-surface temperatures. *Clim. Dyn.* **14**: 545–569.

Pegion K, Kirtman BP. 2008a. The impact of air-sea interactions on the predictability of the tropical intraseasonal oscillation. *J. Clim.* **21**: 5870–5886.

Pegion K, Kirtman BP. 2008b. The impact of air-sea interactions on the simulation of tropical intraseasonal variability. *J. Clim.* **21**: 6616–6635.

Plaut G, Vautard R. 1994. Spells of low-frequency oscillations and weather regimes in the Northern Hemisphere. *J. Atmos. Sci.* **51**:210–236.

Saha S, Nadiga S, Thiaw C, Wang J, Wang W, Zhang Q, Van den Dool HM, Pan H-L, Moorthi S, Behringer D, Stokes D, Peña M, Lord S, White G, Ebisuzaki W, Peng P, Xie P. 2006. The NCEP Climate Forecast System. *J. Clim.* **19**: 3483–3517.

Saha S, Moorthi S, Pan H-L, Wu X, Wang J, Nadiga S, Tripp P, Kistler R, Woollen J, Behringer D, Liu H, Stokes D, Grumbine R, Gayno G, Wang J, Hou Y-T, Chuang H-Y, Juang H-MH, Sela J, Iredell M, Treadon R, Kleist D, Van Delst P, Keyser D, Derber J, Ek M, Meng J, Wei H, Yang R, Lord S, Van den Dool H, Kumar A, Wang W, Long C, Chelliah M, Xue Y, Huang B, Schemm J-K, Ebisuzaki W, Lin R, Xie P, Chen M, Zhou S, Higgins W, Zou C-Z, Liu Q, Chen Y, Han Y, Cucurull L, Reynolds RW, Rutledge G, Goldberg

M. 2010. The NCEP Climate Forecast System Reanalysis. *Bull. Amer. Meteorol. Soc.* **91**: 1015–1057.

Saha S, Moorthi S, Wu X, Wang J, Nadiga S, Tripp P, Behringer D, Hou Y-T, Chuang H-Y, Iredell M, Ek M, Meng J, Yang R, Mendez MP, Van den Dool H, Zhang Q, Wang W, Chen M, Becker E. 2014. The NCEP Climate Forecast System Version 2. *J. Clim.* **27**: 2185–2208.

Sikka DR, Gadgil S. 1980. On the maximum cloud zone and the ITCZ over Indian longitudes during the southwest monsoon. *Mon. Wea. Rev.* **108**: 1840–1853.

Sperber KR. 2003. Propagation and the vertical structure of the Madden-Julian Oscillation. *Mon. Wea. Rev.* **131**: 3018–3037.

Sperber KR, Annamalai H. 2008. Coupled model simulations of boreal summer intraseasonal (30-50 day) variability, Part I: Systematic errors and caution on use of metrics. *Clim. Dyn.* **31**: 345–372.

Sperber KR, Annamalai H, Kang I-S, Kitoh A, Moise A, Turner A, Wang B, Zhou T. 2013. The Asian summer monsoon: an intercomparison of CMIP5 vs. CMIP3 simulations of the late 20th century. *Clim. Dyn.* **41**: 2711–2744.

Waliser DE, Jin K, Kang I-S, Stern WF, Schubert SD, Wu MLC, Lau K-M, Lee M-I, Krishnamurthy V, Kitoh A, Meehl GA, Galin VY, Satyan V, Mandke SK, Wu G, Liu Y, Park C-K. 2003. AGCM simulations of intraseasonal variability associated with the Asian summer monsoon. *Clim. Dyn.* **21**: 423–446.

Wang B, Ding Q, Fu X, Kang I-S, Jin K, Shukla J, Doblas-Reyes F. 2005. Fundamental

challenge in simulation and prediction of summer monsoon rainfall, *Geophys. Res. Lett.* **32**: L15711. doi:10.1029/2005GL022734.

Wang W, Hung M-P, Weaver SJ, Kumar A, Fu X. 2014. MJO prediction in the NCEP Climate Forecast System version 2. *Clim. Dyn.* **42**: 2509–2520.

Yasunari T. 1979. Cloudiness fluctuations associated with the northern hemisphere summer monsoon. *J. Meteorol. Soc. Japan* **57**: 227–242.

Zhang C. 2005. Madden-Julian Oscillation. *Rev. Geophys.* **43**: RG2003. doi:10.1029/2004RG000158.

Figure captions

Fig. 1. JJAS seasonal climatological mean of precipitation in (a) observation (TRMM) and (b) May forecasts of the model (CFSv2), and standard deviation of daily mean precipitation during JJAS season in (d) observation and (e) May forecasts of the model. DJFM seasonal climatological mean of precipitation in (f) observation (TRMM) and (g) November forecasts of the model and standard deviation of daily mean precipitation during DJFM season in (i) observation and (j) November forecasts of the model. Difference in climatological mean between model and observation for (c) JJAS and (h) DJFM seasons. Units are in mm day^{-1}.

Fig. 2. Active composite minus break composite of daily precipitation anomalies during JJAS season in (a) observation (TRMM) and (b) model's May forecasts. The active and break periods used in the composites are based on the EIMR index of observation in (a) and EIMR index of model forecasts in (b). The EIMR index is the average of precipitation anomaly over the domain (70°E–100°E, 10°N–30°N) shown as green box in (a). The model composite based on EIMR index in observation (TRMM) is shown in (c). The active and break periods used in (c) are same as those used in (a). Active composite minus break composite of daily precipitation anomalies during DJFM season in (d) observation (TRMM) and (e) model's November forecasts. The active and break periods used in the composites are based on the MAMR index of observation in (d) and MAMR index of model forecasts in (e). The MAMR index is the average of precipitation anomaly over the domain (110°E–150°E, 20°S–0°) shown as green box in (d). The model composite based on MAMR index in observation (TRMM) is shown in (f). The active and break periods used in (f) are same as those used in (d). The model composites are averages

of all the ensemble members. Units are in mm day^{-1}.

Fig. 3. Power spectra of ISO in TRMM observation (red) and in the ensemble members of the model forecasts (blue) for (a) boreal summer and (b) boreal winter. The model forecasts are from May initial conditions in (a) and from November initial conditions in (b). Standard deviation of daily RC of MISO in (c) observation and (e) May forecasts of the model, and (g) difference in the standard deviation between the model and observation for boreal summer. Standard deviation of daily RC of MJO in (d) observation and (f) November forecasts of the model and (h) difference in the standard deviation between the model and observation for boreal winter. Units are in mm day^{-1}.

Fig. 4. Phase composites of precipitation RC for four phase intervals of ISO cycle in (a) TRMM observation and (b) model forecasts for boreal summer. The phase number is given at the top right corner of each panel. The model forecasts are from May initial conditions. The phase composites are averages of composites of all the ensemble members of the forecasts. Units are in mm day^{-1}.

Fig. 5. Longitude-phase cross-section of the phase composites of the RC of MISO averaged over 10°S–10°N in (a) observation and (c) model forecasts, and latitude-phase cross-section of the phase composites of the RC of MISO averaged over 65°E–95°E in (b) observation and (d) model forecasts for boreal summer. The model forecasts are from May initial conditions. Units are in mm day^{-1}.

Fig. 6. Phase composites of precipitation RC for four phase intervals of ISO cycle in (a) TRMM observation and (b) model forecasts for boreal winter. The phase number is given at the

top right corner of each panel. The model forecasts are from November initial conditions. The phase composites are averages of composites of all the ensemble members of the forecasts. Units are in mm day^{-1}.

Fig. 7. Longitude-phase cross-section of the phase composites of the RC of MJO averaged over 10°S–10°N in (a) observation and (c) model forecasts, and latitude-phase cross-section of the phase composites of the RC of MJO averaged over 90°E–120°E in (b) observation and (d) model forecasts for boreal winter. The model forecasts are from November initial conditions. Units are in mm day^{-1}.

Fig. 8. (a) EIMR index of the RC of MISO in TRMM observation (red) and individual ensemble members of the model forecasts from May initial conditions (blue) for 2001. (b) Same as (a) but shown for forecasts from initial conditions of 6 May and 16 May only. (c) MAMR index of the RC of MJO in TRMM observation (red) and individual ensemble members of the model forecasts from November initial conditions (blue) for 2001–2002.

Fig. 9. Phase composites of total anomalies of zonal wind at 850 hPa for four phase intervals of MISO cycle in (a) TRMM observation and (b) model forecasts for boreal summer. The phase number is given at the top right corner of each panel. The model forecasts are from May initial conditions. The phase composites are averages of composites of all the ensemble members of the forecasts. Units are in m s^{-1}.

Fig. 10. Phase composites of total anomalies of zonal wind at 850 hPa for four phase intervals of MJO cycle in (a) TRMM observation and (b) model forecasts for boreal winter. The phase number is given at the top right corner of each panel. The model forecasts are from

November initial conditions. The phase composites are averages of composites of all the ensemble members of the forecasts. Units are in m s^{-1}.

Fig. 11. Phase composites of total anomalies of OLR for four phase intervals of (a) the MISO cycle during the boreal summer and (b) the MJO cycle during boreal winter in the model forecasts. The phase number is given at the top right corner of each panel. The model forecasts are from (a) May and (b) November initial conditions. The phase composites are averages of composites of all the ensemble members of the forecasts. Units are in W m^{-2}.

Fig. 12. Longitude-phase cross-section (shaded) of the phase composites of total anomalies of vorticity at 850 hPa averaged over 10°S–10°N in (a) observation and (b) model forecasts, and latitude-phase cross-section (shaded) of the phase composites of total anomalies of vorticity at 850 hPa averaged over 65°E–95°E in (c) observation and (d) model forecasts for boreal summer. The model forecasts are from May initial conditions. The unit of vorticity is 10^{-6} s^{-1}.The corresponding cross-sections of the precipitation RC of MISO are also plotted as contours at an interval of 0.8 mm day^{-1}. Positive (negative) values are plotted as solid (dashed) contours.

Fig. 13. Longitude-phase cross-section (shaded) of the phase composites of total anomalies of divergence at 200 hPa averaged over 10°S–10°N in (a) observation and (b) model forecasts, and latitude-phase cross-section (shaded) of the phase composites of total anomalies of divergence at 200 hPa averaged over 65°E–95°E in (c) observation and (d) model forecasts for boreal summer. The model forecasts are from May initial conditions. The unit of divergence is 10^{-6} s^{-1}.The corresponding cross-sections of the precipitation RC of MISO are also plotted as

contours at an interval of 0.8 mm day^{-1}. Positive (negative) values are plotted as solid (dashed) contours.

Fig. 14. Longitude-phase cross-section (shaded) of the phase composites of total anomalies of vorticity at 850 hPa averaged over 10°S–10°N in (a) observation and (b) model forecasts, and latitude-phase cross-section (shaded) of the phase composites of total anomalies of vorticity at 850 hPa averaged over 90°E–120°E in (c) observation and (d) model forecasts for boreal winter. The model forecasts are from November initial conditions. The unit of vorticity is 10^{-6} s^{-1}.The corresponding cross-sections of the precipitation RC of MJO are also plotted as contours at an interval of 0.8 mm day^{-1}. Positive (negative) values are plotted as solid (dashed) contours.

Fig. 15. Longitude-phase cross-section (shaded) of the phase composites of total anomalies of divergence at 200 hPa averaged over 10°S–10°N in (a) observation and (b) model forecasts, and latitude-phase cross-section (shaded) of the phase composites of total anomalies of divergence at 200 hPa averaged over 90°E–120°E in (c) observation and (d) model forecasts for boreal winter. The model forecasts are from November initial conditions. The unit of divergence is 10^{-6} s^{-1}.The corresponding cross-sections of the precipitation RC of MJO are also plotted as contours at an interval of 0.8 mm day^{-1}. Positive (negative) values are plotted as solid (dashed) contours.

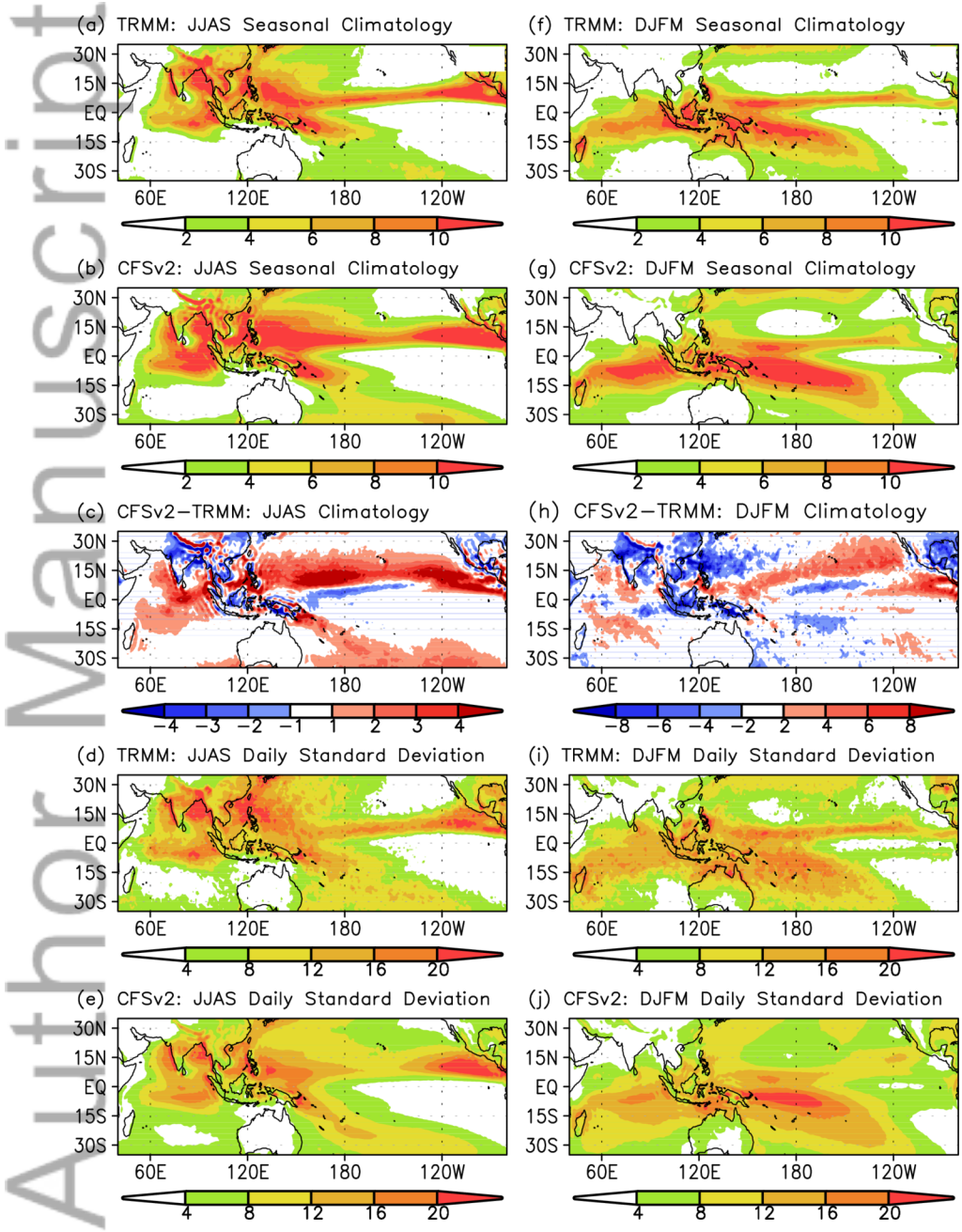

figure_01

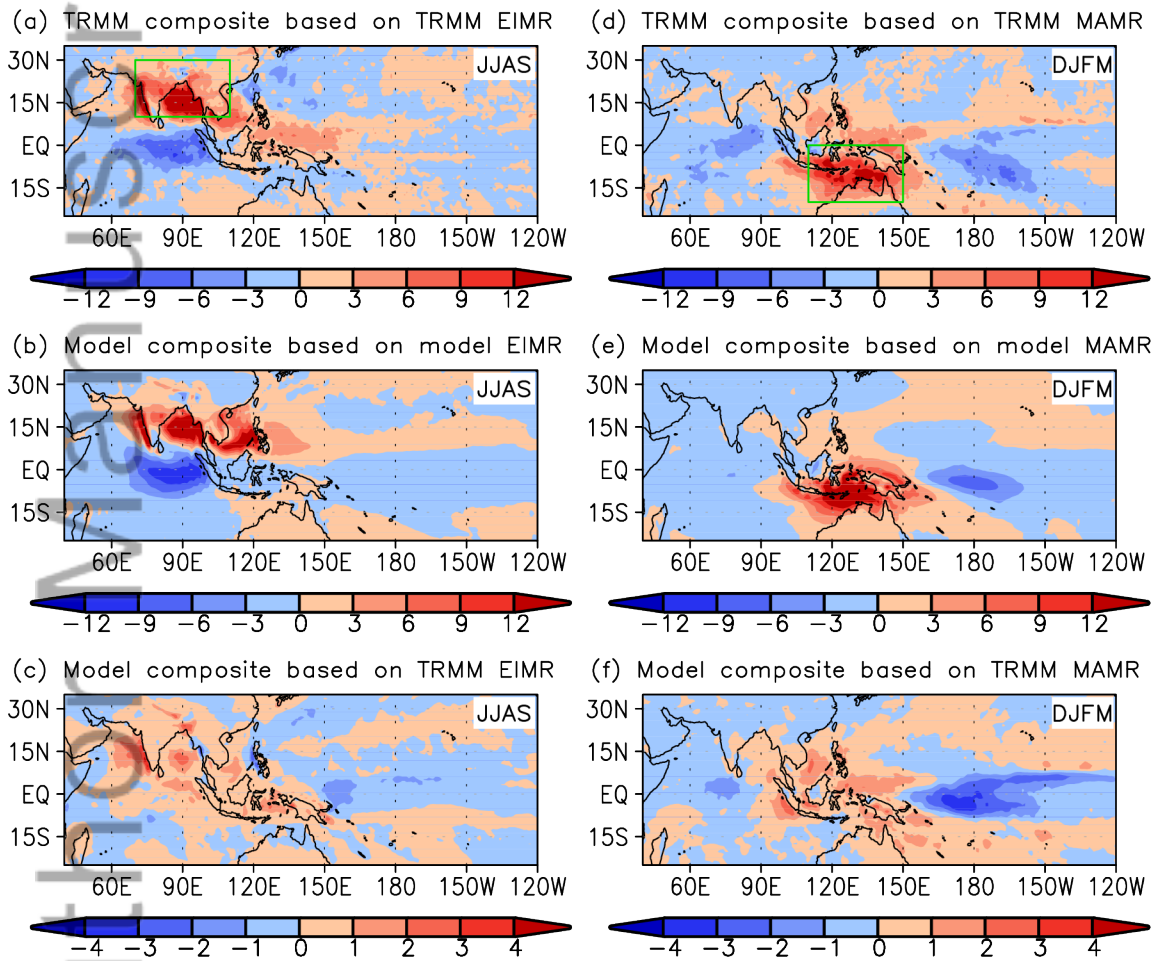

figure_02

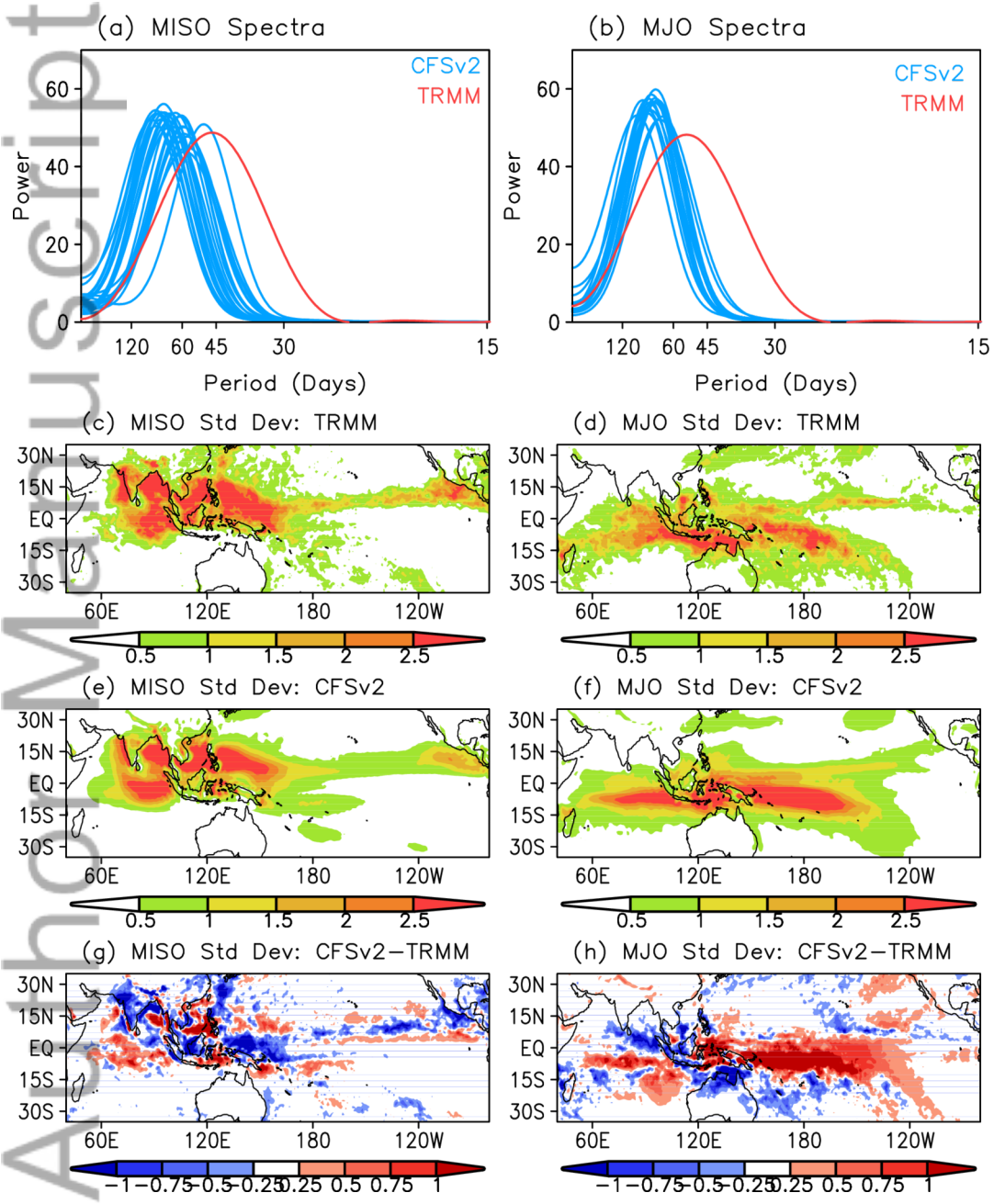

figure_03

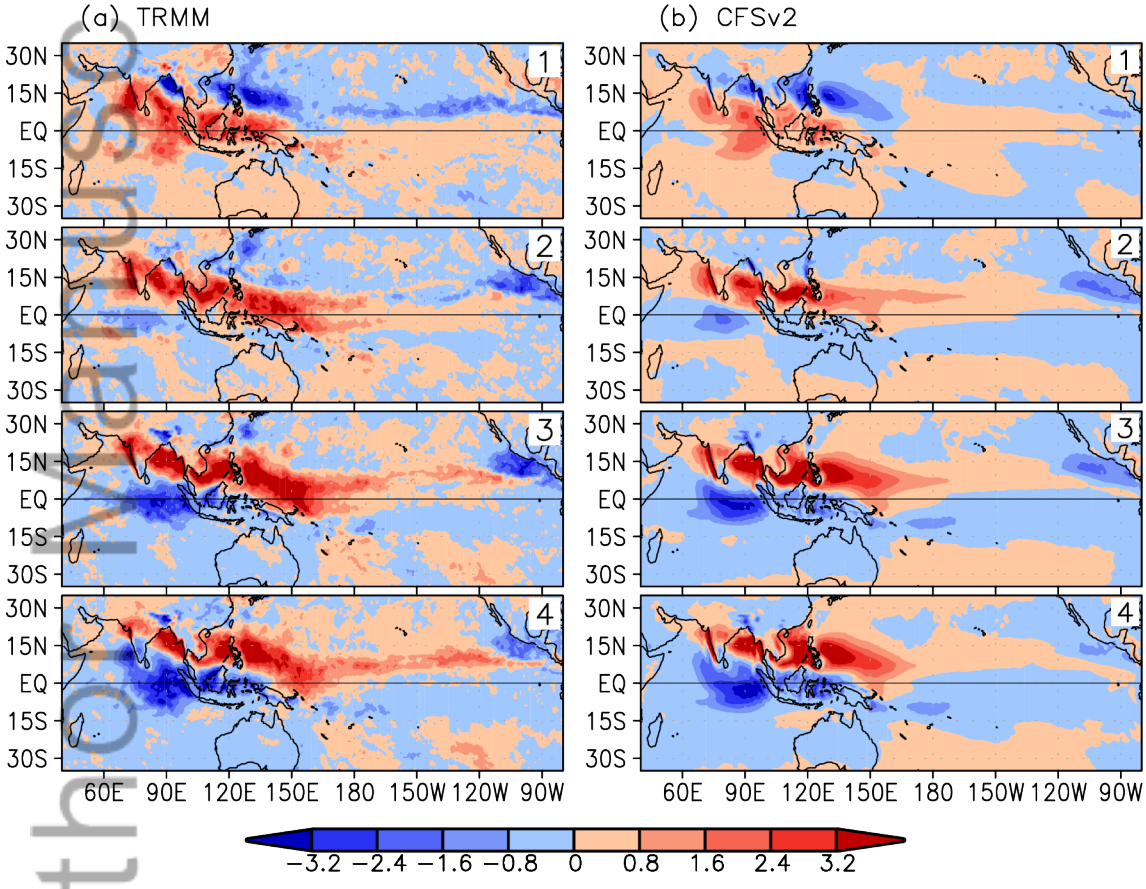

figure_04

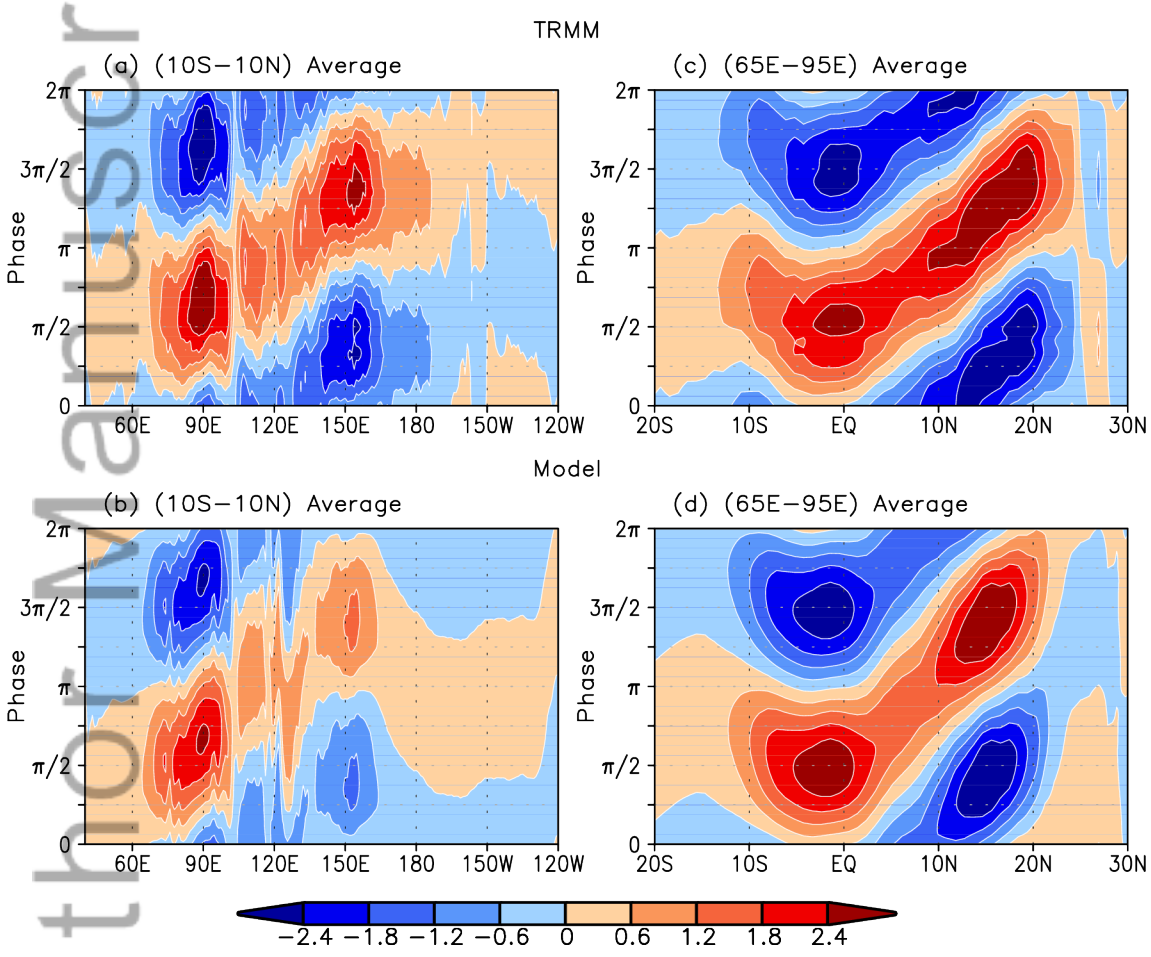

figure_05

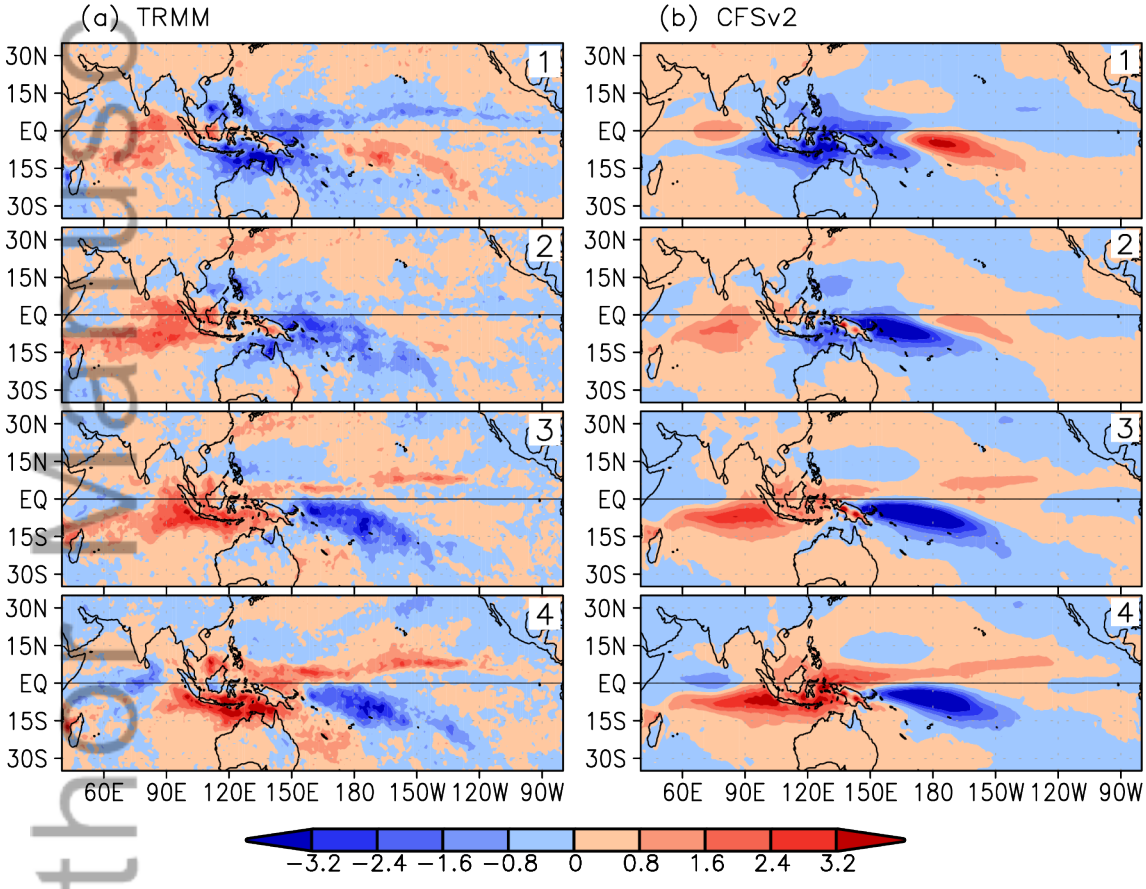

figure_06

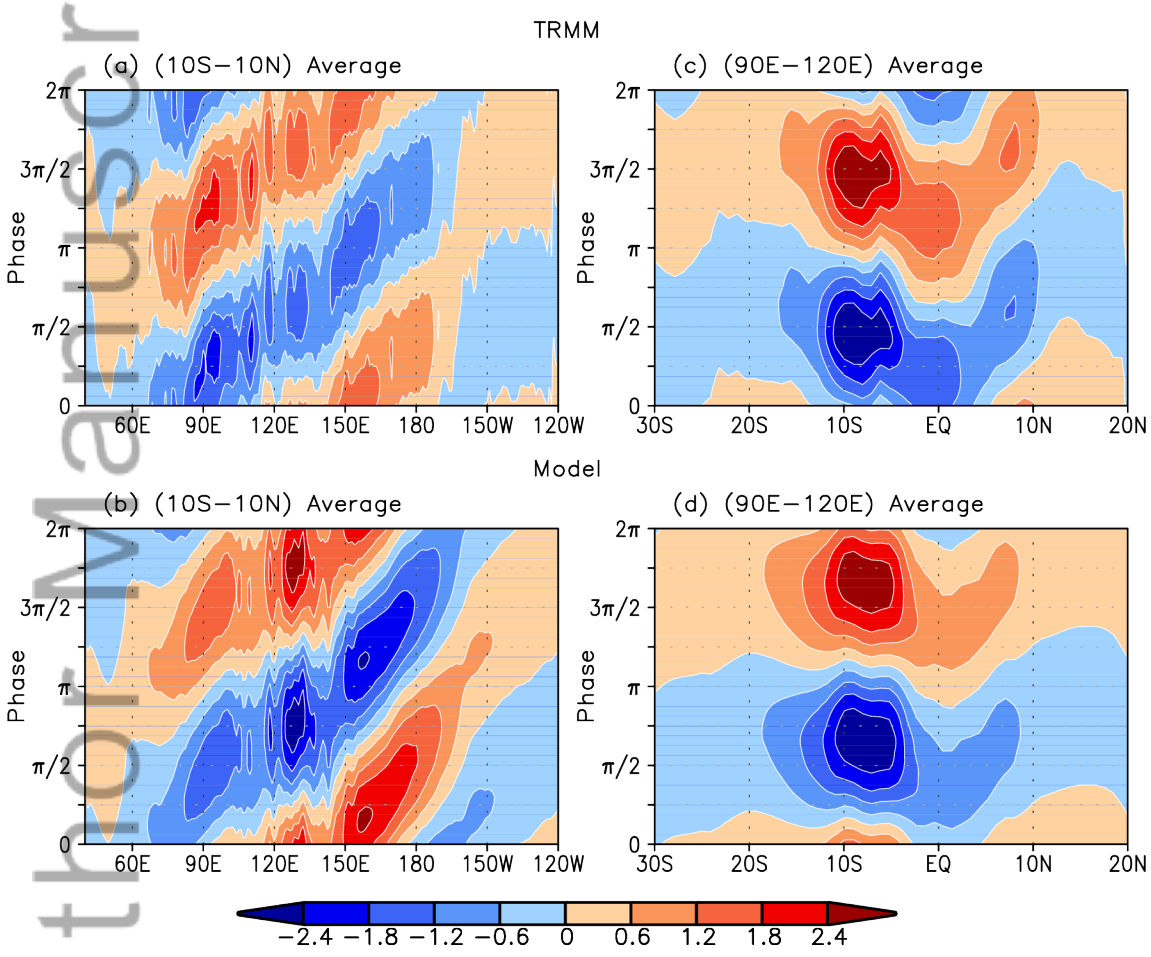

figure_07

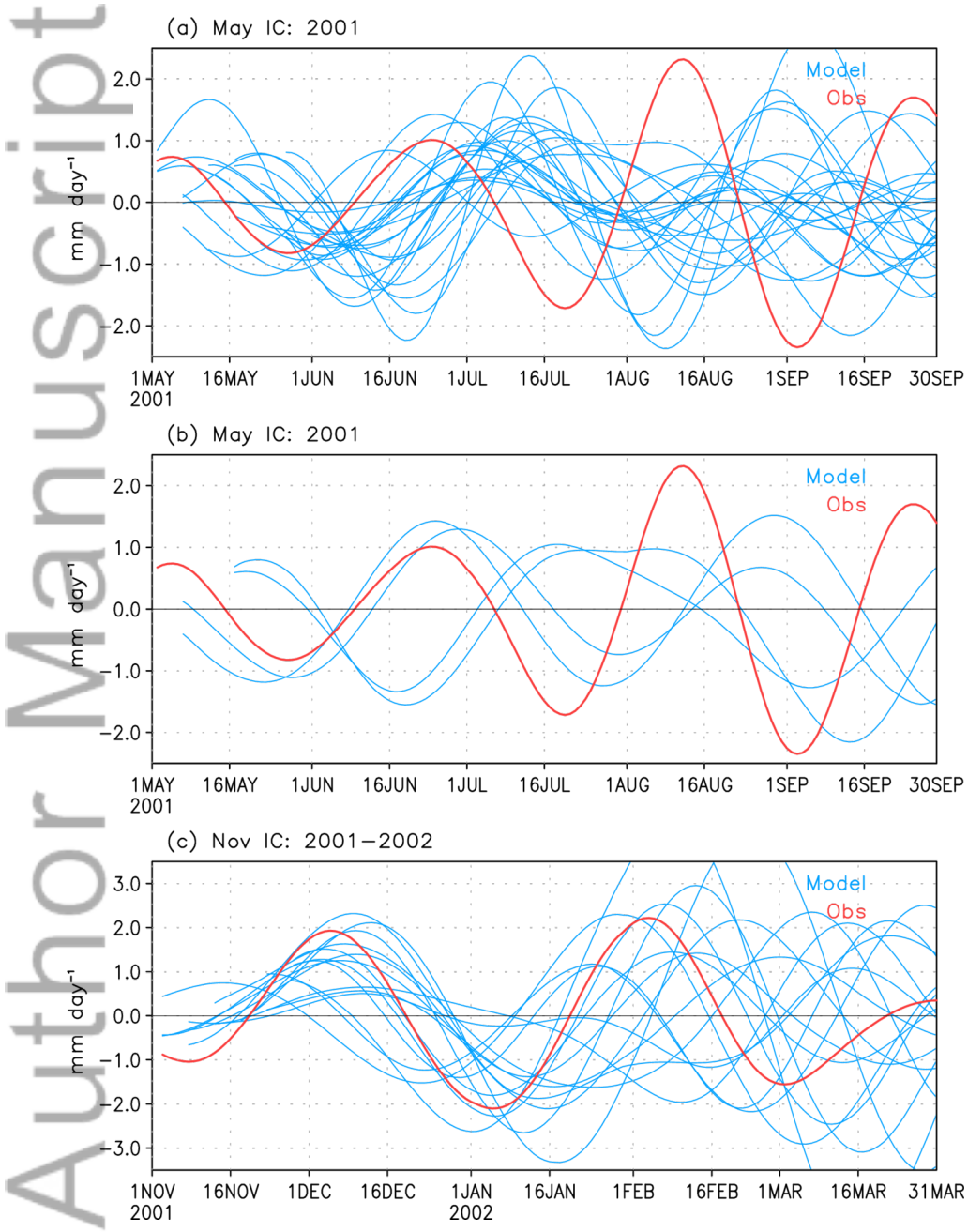

figure_08

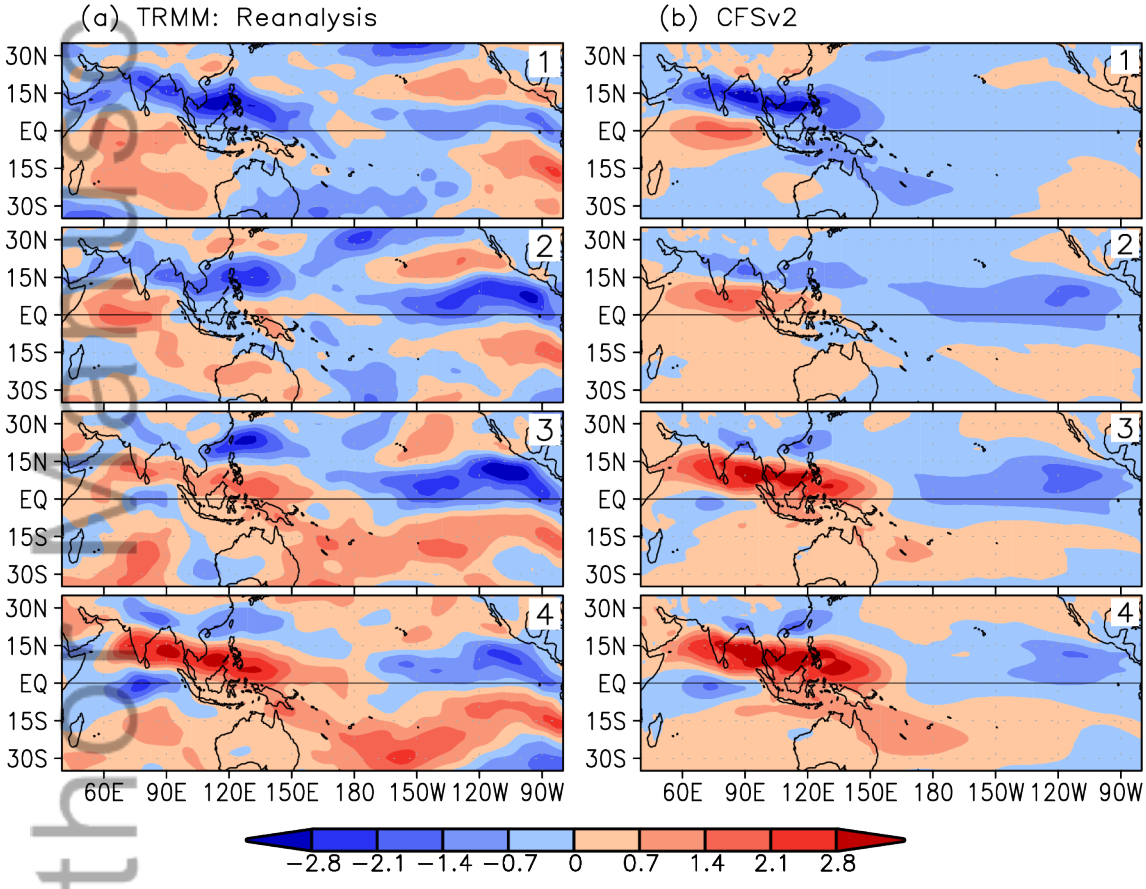

figure_09

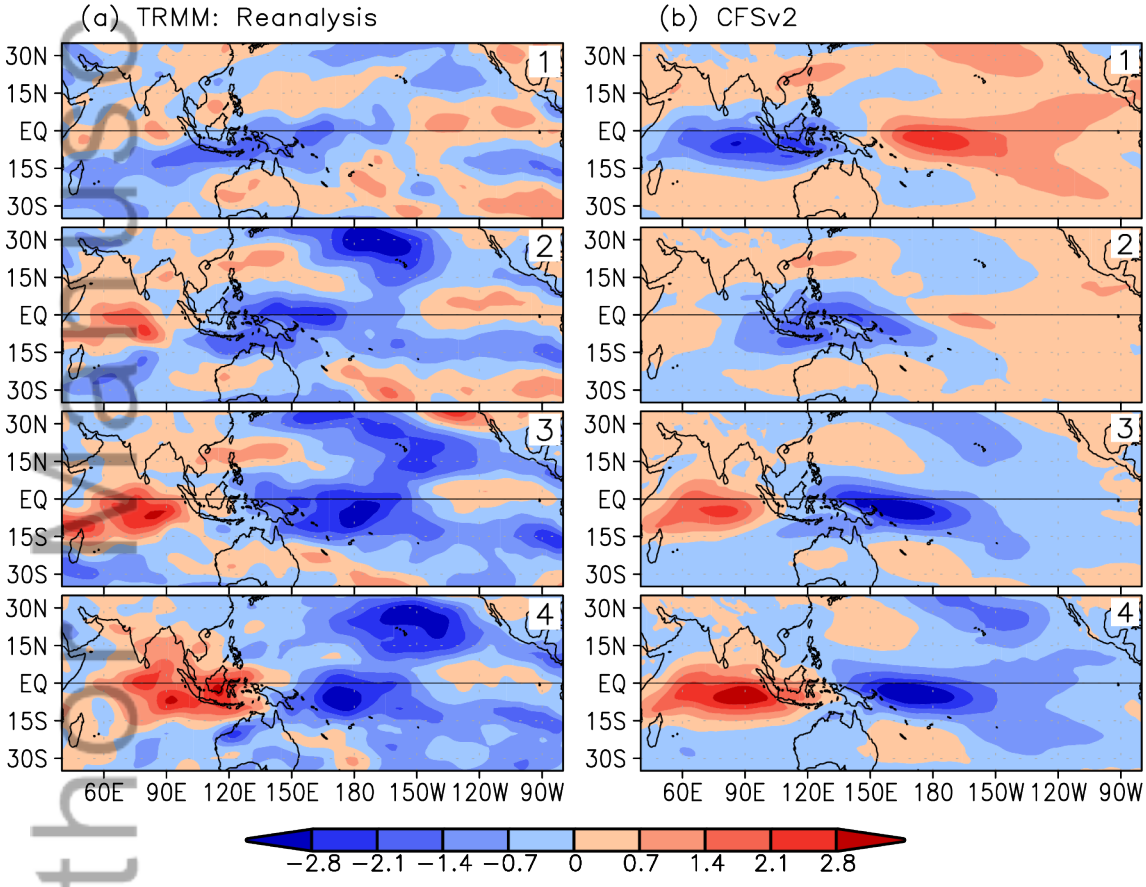

figure_10

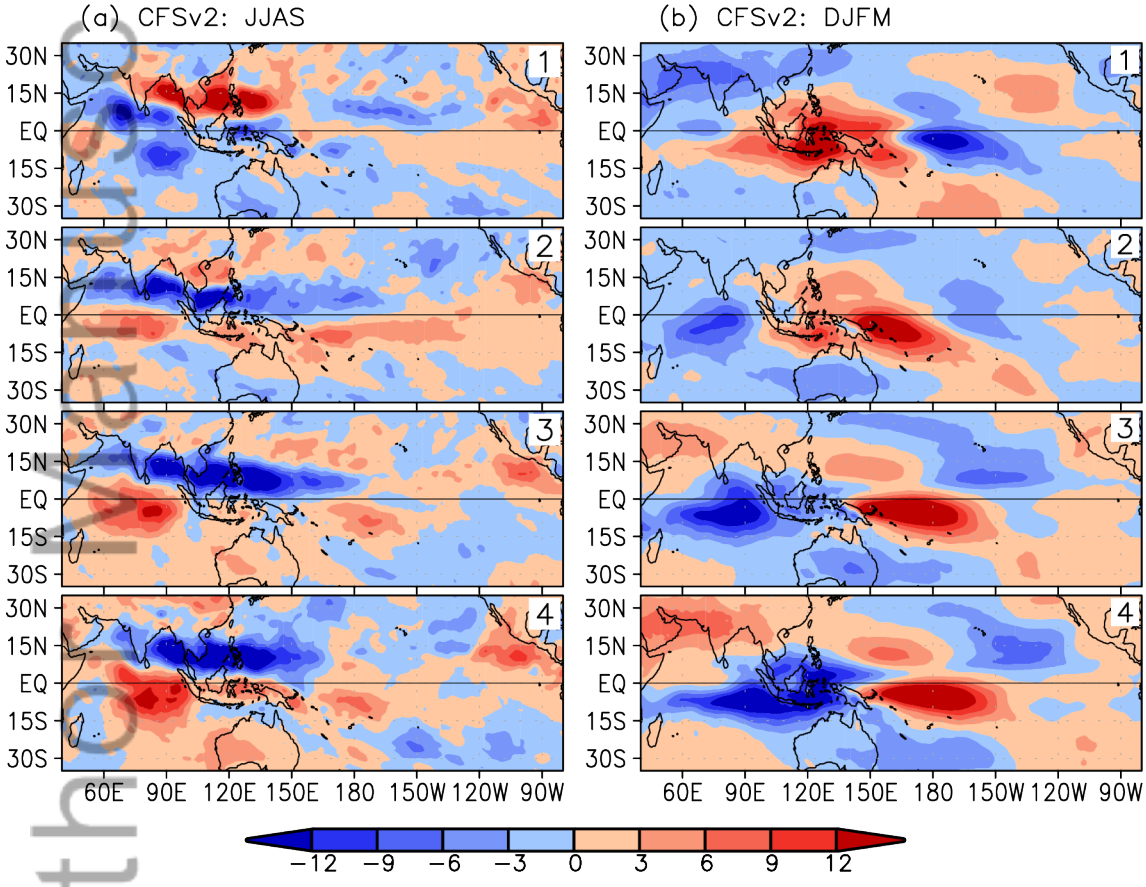

figure_11

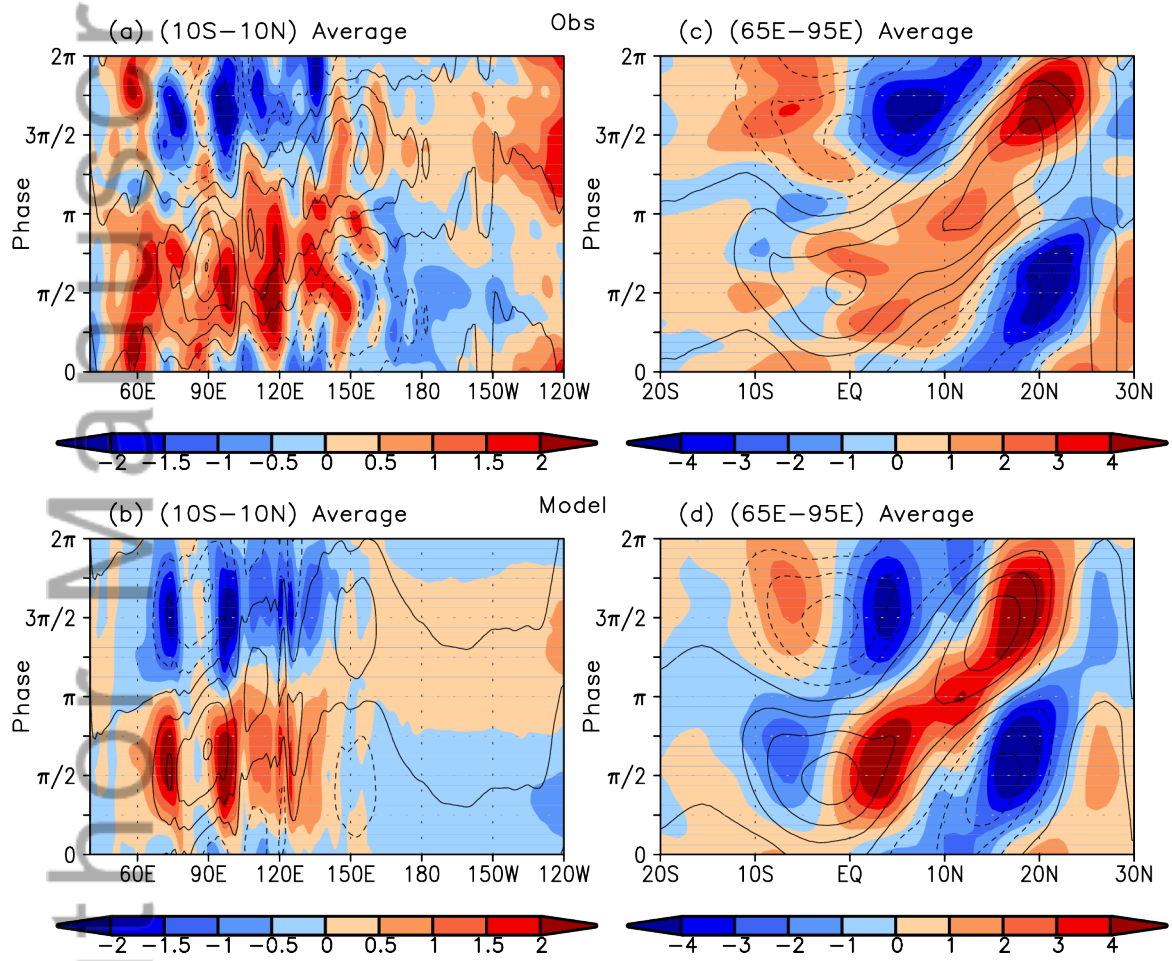

figure_12

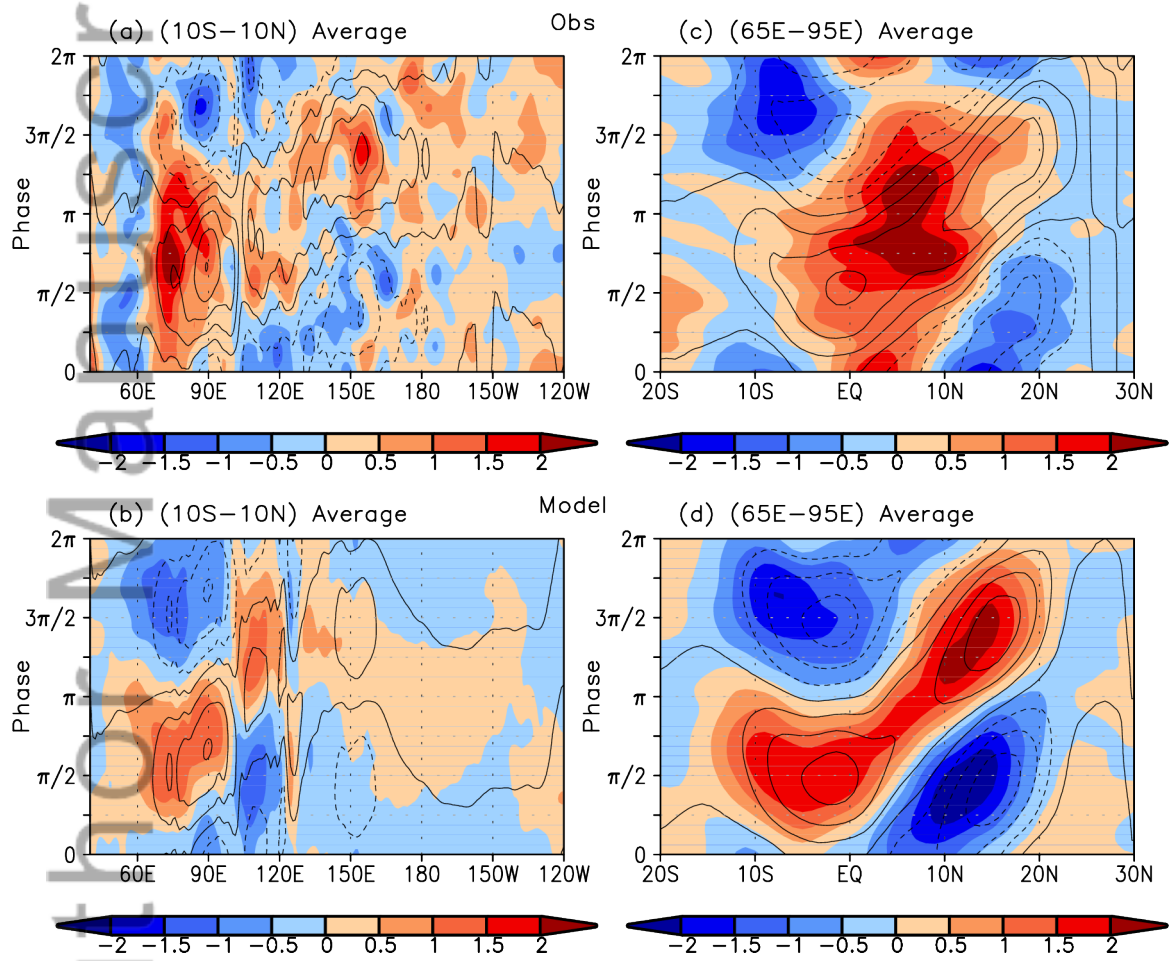

figure_13

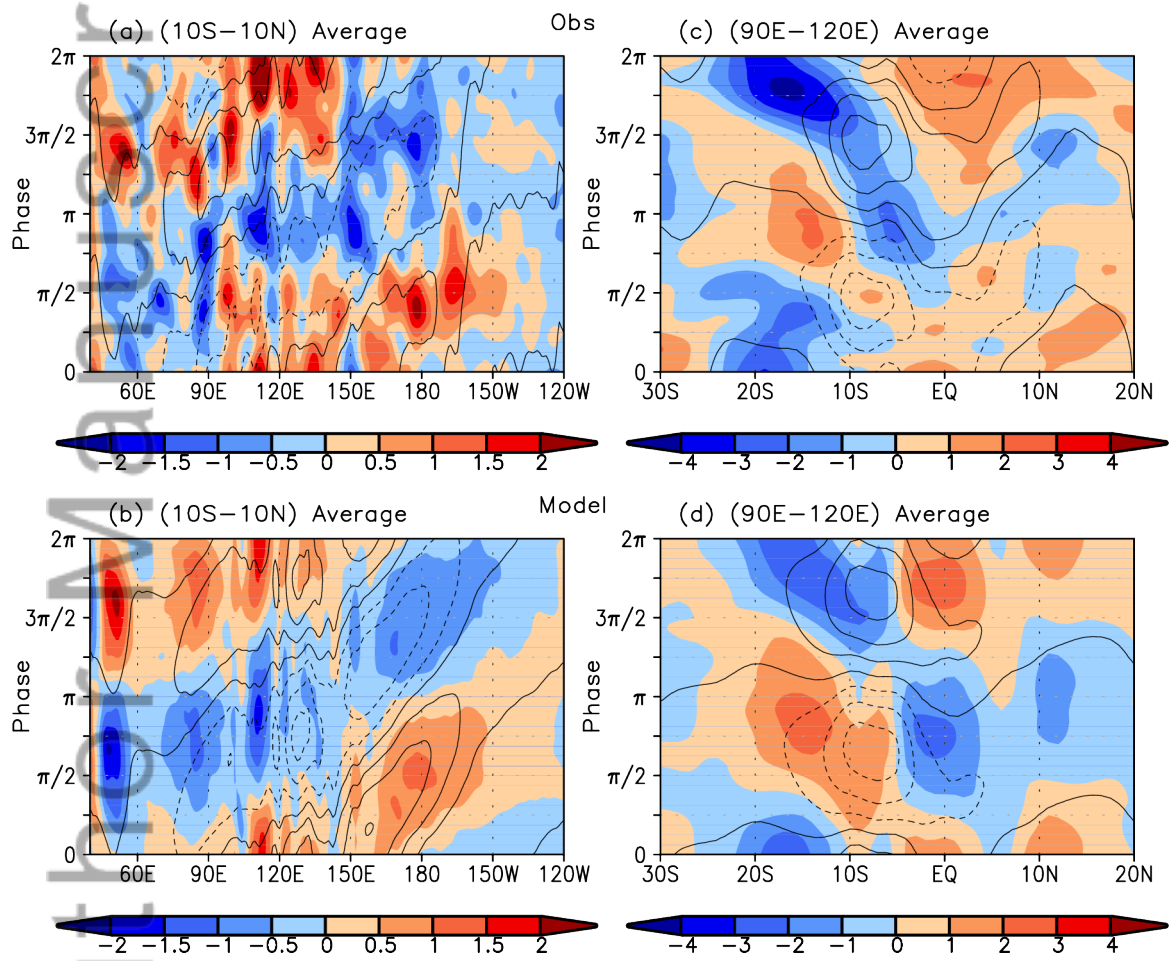

figure_14

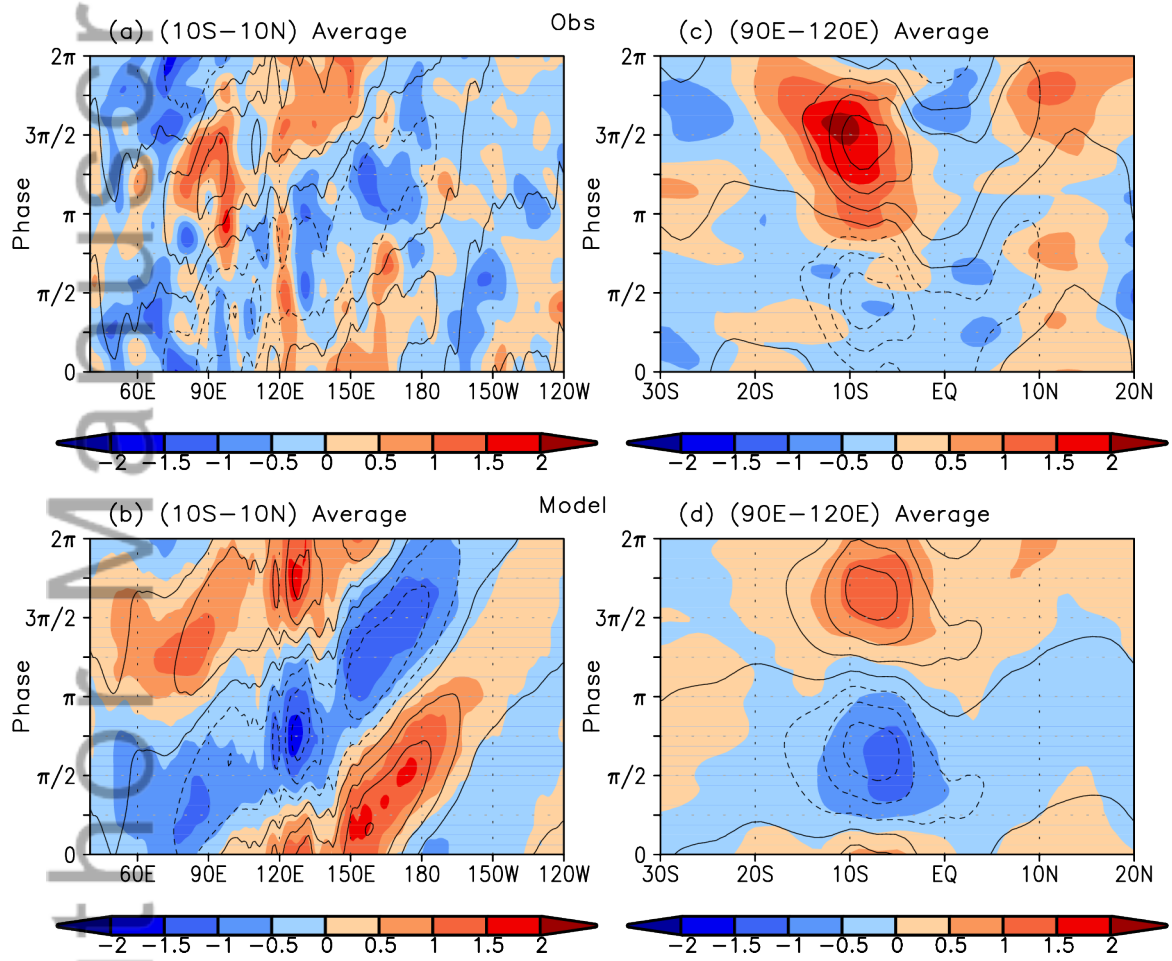

figure_15

Tropical Intraseasonal Oscillations in CFSv2 during Boreal Summer and Winter

Running Head: Intraseasonal Oscillations in CFSv2

V. Krishnamurthy

Center for Ocean-Land-Atmosphere Studies
George Mason University
Fairfax, Virginia

Revised
September 2016

Corresponding author:
V. Krishnamurthy
Center for Ocean-Land-Atmosphere Studies
Research Hall, MS 6C5
George Mason University
4400 University Drive
Fairfax, VA 22030
E-mail: vkrishna@gmu.edu

Abstract

The simulation of the tropical intraseasonal oscillations (ISOs) by a coupled model in the Indo-Pacific region is examined in this study. The retrospective forecasts by the Climate Forecast System version 2 (CFSv2) of National Centers of Environmental Prediction for the period 1982–2010 have been analyzed and compared with observation. The leading Indian monsoon intraseasonal oscillation (MISO) during the boreal summer and the Madden-Julian Oscillation (MJO) during the boreal winter are extracted from daily precipitation anomalies in forecasts and observations by using a data-adaptive method. The model forecasts from May initial conditions simulates the observed spatial structure, magnitude and the northward and eastward propagation of MISO reasonably well. Similar performance is also evident in the simulation of the eastward propagating MJO in forecasts from November initial conditions. In the simulation of both the MISO and MJO by the model, the zonal wind at lower level shows appropriate observed relation with the precipitation and coupling with convection. The observed phase relations between precipitation and low-level relative vorticity and between precipitation and upper-level divergence in the zonal and meridional propagations are captured by the model. However, the variance of the ISOs differs from observation in certain regions, and the phase of the ISOs exhibits wide differences among the ensemble members of the forecast and with the observation. Comparison with the earlier model, CFS version 1, shows that the space-time structure and evolution of MISO and MJO are better simulated by CFSv2.

Keywords: Indian monsoon, Intraseasonal oscillation, MISO, MJO, CFSv2, Forecasts

1. Introduction

The tropical climate system in the Indo-Pacific region exhibits strong variability at intraseasonal time scale. The active-break cycle in the Indian monsoon during the boreal summer and the Madden-Julian Oscillation (MJO) during the boreal winter are major manifestations of the tropical intraseasonal variability (e.g., Krishnamurthy and Kinter, 2003; Zhang, 2005). In the Indian region, the active phase of the monsoon brings above-normal rainfall whereas the break phase leads to below-normal or no rainfall (Krishnamurthy and Shukla, 2000). The active (break) period coincides with the strengthening (weakening) of the mean monsoon circulation. The active phase starts with convective activity in the western equatorial Indian Ocean and propagates northward (Sikka and Gadgil, 1980) as well as eastward. The break phase is similar to the active phase but with the movement of suppressed convection zone. The intraseasonal variability of the Indian monsoon has been identified by several studies to occur in the range of 10–90 days (e.g., Yasunari, 1979; Lau and Chan, 1986). The active-break cycle actually consists of intraseasonal oscillations (ISOs) of different periods (Annamalai and Slingo, 2001; Krishnamurthy and Shukla, 2007). The leading monsoon ISO (MISO) has a broad-band spectrum centered at 45 days in convection (Annamalai and Sperber, 2005; Krishnamurthy and Shukla, 2008), rainfall (Krishnamurthy and Shukla, 2007), circulation (Krishnamurthy and Achuthavarier, 2012) and diabatic heating (Hazra and Krishnamurthy, 2015) with strong northward and eastward propagation. During the boreal winter, the MJO is stronger and consists of coupled convection and atmospheric circulation propagating eastward from the equatorial Indian Ocean to the Pacific Ocean (Madden and Julian, 1971, 1972, 1994; Zhang, 2005).

Although considerable progress has been made in modeling the tropical climate, the simulation and prediction of the tropical ISOs are still challenging (e.g., Kim *et al*., 2009;

Sperber *et al*., 2013; Hung *et al*., 2013). The atmospheric general circulation models forced by observed sea surface temperature (SST) were found to produce ISOs which were less coherent with inadequate spatial extent and lacked proper eastward and northward propagation (Waliser *et al.*, 2003). The lack of variability over the oceanic region and the inaccurate phases of the simulated ISOs pointed to the importance of proper SST feedback (Kang *et al*., 2002). Based on controlled model experiments, Wang *et al*. (2005) suggested that coupled ocean-atmosphere models are necessary for better simulation of the monsoon rainfall. During the past decade, the usage of coupled models has become more common, and has led to organized assessment of coupled models. In the Coupled Model Intercomparison Project-3 (CMIP3), the MJO in most of the models had low variance and lacked coherent eastward propagation (Lin *et al*., 2006). However, the models from the later project CMIP5 showed improvement in MJO by generating larger variance and somewhat better spectral peak but were still unable to simulate realistic eastward propagation (Hung *et al*., 2013). The simulation of the life cycle of the boreal summer ISO over the monsoon region was found to be inadequate in CMIP3 models although the models showed eastward propagation (Sperber and Annamalai, 2008). Sperber *et al*. (2013) compared CMIP3 and CMIP5 models and found that the northward propagation was improved in several later models although major problems still exist in the simulation of the intraseasonal variability of the summer monsoon.

Coupled climate models are employed at major operational forecast centers for subseasonal and seasonal predictions. The National Centers for Environmental Prediction (NCEP) has been providing seasonal forecasts with the Climate Forecast System version 1 (CFSv1) since 2004 (Saha *et al*., 2006) and with the upgraded CFS version 2 (CFSv2) since 2011 Saha *et al*., 2014). The CFSv2 includes improvements in the atmospheric and oceanic

components of the model and in the data assimilation systems. The study by Wang *et al*. (2014) showed that the MJO prediction skill of CFSv2 has improved in comparison to CFSv1 while systematic errors are still present. The boreal summer MISO simulated by CFSv1 was found to have much longer period and less variance compared to observations but exhibited northeastward propagation (Achuthavarier and Krishnamurthy, 2011a). The SST variability and the ocean-atmosphere interaction in the Indian Ocean are important in properly simulating the propagation of MISO (Achuthavarier and Krishnamurthy, 2011b). Similarly, through experiments with CFSv1, Pegion and Kirtman (2008a, 2008b) concluded that the MJO during the boreal winter was better simulated when the air-sea interaction occurred through proper variation of SST at daily and intraseasonal time scales. The importance of air-sea interaction was also pointed out by other model studies in MISO (Fu *et al*., 2003) and MJO (Klingaman and Woolnough 2014).

The objective of this study is to investigate the performance of CFSv2 in simulating the leading tropical ISO during boreal summer and winter. The spatial structure, period and the propagation properties of the leading MISO and MJO simulated by CFSv2 will be analyzed to determine if any improvements have occurred compared to the simulations of CFSv1. The associated circulation features and possible mechanisms involving circulation will also be examined. For this purpose, the nine-month long retrospective forecasts of CFSv2 generated by NCEP with a series of different initial conditions will be used. The MISO during the boreal summer and MJO during the boreal winter will be extracted in precipitation by using a suitable data-adaptive method. The spatial structure of MISO is known to extend into the Pacific in observations (Krishnamurthy and Shukla, 2008), and the eastward propagation of MJO into the Pacific is also well-known (Madden and Julian, 1994). Therefore, the domain used in this study will cover the entire tropical Indo-Pacific region.

The model and its forecasts, observed data and the method of analysis are described in section 2. In section 3, the mean climate and the extraction of the summer and winter ISOs will be described. Section 4 discusses the space-time evolution of the precipitation ISOs and the relation with circulation. Summary and conclusions are provided in section 5.

2. Model, data and method of analysis

2.1. Model and data

The CFSv2 is a globally coupled model currently used for operational seasonal forecasts by the NCEP. The atmospheric component is based on the NCEP Global Forecast System (GFS), and has 64 vertical levels and T126 horizontal resolution (nearly 100 km grid spacing). The ocean component is the Geophysical Fluid Dynamics Laboratory (GFDL) Modular Ocean Model version 4 (MOM4) with 40 vertical levels and 0.5° horizontal resolution which increases meridionally to 0.25° in the deep tropics. The CFSv2 includes Noah land model and GFDL Sea Ice Simulator. More details of CFSv2 and the modifications introduced are described by Saha *et al*. (2010, 2014).

This study has used the nine-month retrospective forecasts generated by the NCEP. The forecasts are made from initial conditions of every fifth day starting from 1 January of every year during 1982–2010. On each initial day, an ensemble of four forecasts is generated from initial conditions of 0000, 0600, 1200 and 1800 UTC. In this study, the forecasts made from May and November initial conditions are used for analyzing, respectively, the boreal summer MISO and boreal winter MJO. The May forecasts in each year consist of an ensemble of 28 members starting from four initial conditions each on 1, 6, 11, 16, 21, 26 and 31 May during 1982–2010.

In the November forecasts, an ensemble of 24 forecasts in each year is obtained from four initial conditions on 2, 7, 12, 17, 22 and 29 November of 1982–2010. The daily mean precipitation and horizontal winds at 850 and 200 hPa from the above forecasts are analyzed. The daily mean precipitation from Version 7 of Tropical Rainfall Measuring Mission (TRMM) 3B42 product on 0.25°×0.25° horizontal grid for the period 1998–2010 (Huffman *et al*., 2007) is used for observation. Although the TRMM data set does not cover the entire period of the forecasts, it has the advantage of including coverage over both and land and ocean. The horizontal wind data were obtained from the CFS Reanalysis (CFSR; Saha *et al*., 2010) for the period 1982–2010.

2.2. Method of analysis

The multi-channel singular spectrum analysis (MSSA; Ghil *et al*., 2002) is the method used in this study to extract the ISOs. This method is the multivariate version of the singular spectrum analysis introduced by Broomhead and King (1986). The MSSA has been successfully used to extract the space-time structure of ISOs in previous studies of monsoon (e.g., Krishnamurthy and Shukla, 2008). Starting with a given time series of data at L grid points (or channels) and N discrete time intervals, a delayed co-ordinate approach is adopted by adding M lagged copies of the data. A grand lagged covariance matrix C is constructed and diagonalized to obtain LM eigenvalues and LM eigenvectors. Each eigenvector contains M lagged patterns and forms the space-time EOF (ST-EOF) while the corresponding space-time principal component (ST-PC) is of time length $N-M+1$. The eigenvalues explain the variance of the eigenmodes. The time series corresponding to each eigenmode is obtained as reconstructed component (RC) by multiplying the corresponding ST-EOF and ST-PC (see Ghil *et al*. 2002 for the formula). The RC is the data-adaptive filter which has the same spatial and time dimensions as the original time

series. By adding all the RCs, the original time series is recovered. The eigenmodes obtained from MSSA can be oscillations, persistent modes or trends. A pair of consecutive eigenmodes with almost degenerate eigenvalues is oscillatory if the corresponding ST-PCs and ST-EOFs are in quadrature and have almost equal period (Plaut and Vautard, 1994; Ghil *et al*., 2002). The ISOs can be extracted by identifying such oscillations which emerge as a pair of eigenmodes. All the MSSA eigenmodes analyzed in this paper were found to be statistical significant at 5% level by following the Monte Carlo test against signals from red noise as discussed by Allen and Robertson (1996) and Allen and Smith (1996).

3. Mean and Intraseasonal oscillations in precipitation

As stated earlier, the boreal summer ISO in the Indo-Pacific region will be studied by analyzing an ensemble of forecasts starting from 28 different initial conditions during May of each year for the period 1982–2010. The analysis will consider the forecasts up to 30 September of each year, spanning the summer monsoon season. For the boreal winter ISO, the ensemble of 24 forecasts starting from different initial conditions in November each year and ending in 31 March of the subsequent year for the period 1982–2010 will be used. A brief description of the mean and standard deviation of the precipitation is useful before discussing the ISOs. The forecasts from May and November initial conditions will be referred to as May and November forecasts for brevity, hereafter. Although retrospective forecasts have been used, the focus of this study is not to test the accuracy of the day-to-day forecasts compared to observations but to examine whether the model has simulated the features of ISOs by examining the statistics of the retrospective forecasts.

3.1. Mean and standard deviation

The climatological mean of precipitation for the June–September (JJAS) season in observation (TRMM) and May forecasts is shown in Fig. 1. The climatology in the observation is the average of 1998–2010 (Fig. 1a) while it is the average over all ensemble members and over the period 1982–2010 in the forecasts (Fig. 1b). The mean rainfall in the observation has large values over the west coast and central part of India, the Bay of Bengal and the Intertropical Convergence Zone (ITCZ) in the Pacific (Fig. 1a). The model has reproduced the observed spatial structure reasonably well in the Indian monsoon region and the Pacific (Fig. 1b). The difference map between the model and observation (Fig. 1c) indicates that the model has deficit rainfall over parts of India and the Maritime Continent but higher values, by up to 4 mm day^{-1}, in the Indian Ocean and the ITCZ in the Pacific. The standard deviation of the daily anomalies of precipitation for JJAS season for observation (TRMM) and May forecasts are plotted in Figs. 1d and 1e, respectively. The standard deviation of the forecasts is calculated by stringing together all the ensemble members (and not of the ensemble mean) for 1982–2010. The spatial structure of the standard deviation in the observation (Fig. 1d) is similar to that of the climatological mean (Fig. 1a). Although the spatial structure of the standard deviation in the forecasts resembles that of the observation, the difference map between the forecasts and observation (figure not shown) indicates that the model underestimates over parts of India, the Maritime Continent, and warm pool and equatorial regions of the Pacific and overestimates over the northern part of the tropical Pacific.

The climatological mean and the daily standard deviation of the precipitation for the boreal winter are also presented in Fig. 1. The climatology and the standard deviation of the December–March (DJFM) season are calculated for observation (TRMM) and November

forecasts in the same manner as in the case of the boreal summer. The larger values in the DJFM climatology of the observation (Fig. 1f) occur in the Southern Indian Ocean, the Maritime Continent, the ITCZ and the South Pacific Convergence Zone (SPCZ). The model is again able to reproduce the observed structure fairly well (Fig. 1g). The difference map between the model and observation (Fig. 1h) indicates that the forecasts have higher values in the southern Indian Ocean and the SPCZ and lower values over the Maritime Continent and Australia. Generally, both during summer and winter, the model produces more mean rainfall over the oceanic region and less over the land regions compared to observation. The standard deviation of the DJFM season in the observation (Fig. 1i) has a spatial structure similar to that of the mean (Fig. 1f). The model (Fig. 1j) captures the observed structure of the standard deviation to a large extent. The difference map between the model and observation (figure not shown) indicates that the standard deviation is lower over the Maritime Continent, ITCZ and Australia and higher over the Southern Indian Ocean and the SPCZ. The model produces more (less) daily activity where the mean is higher (lower) compared to observation both during summer and winter.

3.2. Active-break cycle

The intraseasonal variability in the summer monsoon is manifested through active phases when there is high rainfall and break phases with weak or no rainfall over the Indian region. The intraseasonal variability in the model forecasts is examined by constructing composites of daily precipitation anomalies based on active and break periods over India during JJAS. For this purpose, the extended Indian monsoon rainfall (EIMR) index (Goswami *et al*. 1999), defined as the rainfall averaged over (70°E–110°E, 10°N–30°N), is used. The EIMR index corresponds to a region of intense monsoon activity (Fig. 1a and 1d). The selection of active (break) period is

based on the criterion that the daily EIMR index is above (below) a threshold of one-half the standard deviation of the daily EIMR index for at least five consecutive days. This criterion is the similar to that used by Krishnamurthy and Shukla (2008).

The active and break composites in the observation were computed using TRMM precipitation for JJAS of 1998–2010. The model composites were first constructed for each ensemble member of the May forecasts by identifying the active and break periods from that ensemble member's daily EIMR index for JJAS of 1982–2010, and then the ensemble mean of the composites was computed. The difference between the active and break composites of the daily precipitation anomalies is shown in Fig. 2. The observation composite (Fig. 2a) shows positive anomalies along the west coast and over the central part of India and the Bay of Bengal while negative anomalies are found in the equatorial Indian Ocean and the West Pacific. The north-south dipole structure between 65°E–100°E is an important feature of the active-break cycle and represents a particular phase of northward propagation of the convective activity. The active-break composite of the model forecasts (Fig. 2b) has good correspondence with the observational composite (Fig. 2a) both in the spatial structure and magnitude and captures the dipole structure and the tilted structure of positive anomalies extending from India to the West Pacific. When the composite of the model forecasts is based on the active and break phases of the observation (Fig. 2c), it shows a complete absence of the dipole structure and almost no rainfall activity over the Indian region and the West Pacific. The reason for this difference is that the phase of the daily variability the EIMR index is different in each ensemble member at any given time and different from the phase of the observation's EIMR index.

A similar analysis was performed for the boreal winter with the November forecasts. For identifying the active and break cycles in the winter, an index of precipitation averaged over

(110°E–150°E, 20°S–0°) is used. This index also corresponds to a region of high rainfall activity in both the mean and standard deviation (Figs. 1f and 1i), and will be referred to as the Maritime Continent-Australia monsoon rainfall (MAMR) index. The active minus break composites were constructed with daily precipitation anomalies of observation (TRMM) and November forecasts for DJFM season using MAMR index, in exactly the same manner as in the boreal summer case. The observation composite (Fig. 2d) has positive anomalies over Maritime Continent and northern Australia and weaker negative anomalies to the east and west. This structure represents a particular phase of the eastward propagation of the MJO. The model composite based on the MAMR index of the forecasts (Fig. 2e) shows a good simulation of the observation pattern (Fig. 2d) both in structure and magnitude. However, the model composite based on the MAMR index of observation (Fig. 2f) is not a good representation of the observed pattern although it is able to capture the anomalies of proper sign in its spatial structure, and seems to be slightly better than the summer composite.

3.3. Leading intraseasonal oscillation

The active-break cycle consists of intraseasonal oscillations with different periods. Observational studies of the boreal summer monsoon have indicated that the leading mode of intraseasonal variability is a nonlinear oscillation with a period of 45 days (Krishnamurthy and Shukla 2007, 2008). The MJO is also an oscillation of similar period dominant during the boreal winter (Madden and Julian, 1971, 1972). In view of the results of the previous subsection, it is of interest to investigate the leading mode of intraseasonal variability in the daily forecasts of the model. For this purpose, the daily precipitation anomalies of the observation and forecasts are decomposed by applying MSSA, similar to the method used by Krishnamurthy and Shukla

(2007, 2008). Since this study is assessing both MISO and MJO, the spatial domain is selected to be the entire tropical Indo-Pacific region. The MSSA is applied on daily precipitation anomalies over the domain (40°E–80°W, 35°S–35°N). For the boreal summer, the MSSA was applied on daily anomalies for the period of May to September. The May forecasts consist of 28 ensemble members, each starting with a different initial condition in May. The MSSA was applied separately on each ensemble member for the period 1982–2010. In the case of boreal winter, the MSSA was applied on daily anomalies for the period of November to March, separately for each of the 24 ensemble members of the November forecasts. Similarly, the MSSA was applied on the TRMM observation separately for the boreal summer and winter. A lag window of 61 days at one-day interval was used in all the MSSA. The ST-EOF and ST-PC of each MSSA eigenmode of the ensemble members and observation were found. Using these, the RCs of each eigenmode, which are the MSSA-decomposed components of the total anomalies, were computed.

For each ensemble member in the model forecasts and for observation, the leading oscillation was identified. An oscillation occurs as a pair of consecutive eigenmodes with almost degenerate eigenvalues and with ST-PCs in quadrature. These and other criteria set forth by Plaut and Vautard (1994) were used for the identification of the leading nonlinear oscillation. Further statistical analysis is performed on the RC of the leading ISO identified in each case. A spatial EOF analysis was carried out on the ISO RC of each ensemble member in the models and in the observation, and the power spectrum of the first PC of each RC was obtained. The power spectra are plotted for the summer and winter in Fig. 3a and 3b, respectively. All the spectra are broad band, reflecting the nonlinear character of the ISOs. The central period of the spectrum in the observation for boreal summer MISO is 45 days whereas it ranges from 47 to 70 days with an average period of 61 days in May forecasts (Fig. 3a). In the boreal winter MJO, the spectrum in

the observation has a central period of 54 days while the November forecasts have spectra with period ranging from 60 to 72 days with an average period of 67 days (Fig. 3b). Figure 3 reveals that the model spectra are slightly further apart from the observational spectra and broader in boreal summer compared to the spectra of boreal winter. It is of interest to note that the period of MJO is slightly higher than that of MISO in observation. The leading ISO in the Indian monsoon region during the boreal summer in CFSv1 was found to have a broad-band spectrum centered at 106 days (Achuthavarier and Krishnamurthy, 2011a). The study by Achuthavarier and Krishnamurthy (2011a) was based on a long simulation whereas the present study is based on retrospective forecasts. The comparison is still reasonable since it is the statistics of the ISOs that has been analyzed and because of the ergodic nature of the solutions of dynamical systems such as the model. Therefore, the MISO in CFSv2 seems to have a better representation of the observed period compared to CFSv1. An examination of the power spectra of the EIMR index of the total precipitation anomaly (figure not shown) indicated that the model forecasts are able to capture the observed variation of power with period at all subseasonal time scales.

The standard deviation of the daily RC of the boreal summer MISO is plotted in Figs. 3c and 3e for observation and May forecasts, respectively. The observation (Fig. 3c) has large values in west coast, Bay of Bengal, eastern Indian Ocean and West Pacific while the signal extends up to the west coast of North America. The model's pattern (Fig. 3e) has good resemblance to the observed pattern (Fig. 3c). However, the model's standard deviation is lower over India, Maritime Continent and western equatorial Pacific and higher over parts of Indian and Pacific oceans as revealed by the difference map (Fig. 3g). The standard deviation of the daily RC of the boreal winter MJO in observation and November forecasts are shown in Figs. 3d and 3f, respectively. Large values are seen around the Maritime Continent and in the SPCZ in the

observation (Fig. 3d). The forecasts show a band of large values extending from the Central Indian Ocean to the SPCZ (Fig. 3f). The difference map in Fig. 3h shows that the model overestimates over a large area in the Pacific and a smaller region in the Indian Ocean while showing lesser values in Bay of Bengal, Maritime Continent and Australia. For both observation and forecasts, the standard deviation of the ISOs is about 10–20% (varying spatially) of the corresponding standard deviation of the total mean precipitation shown in Fig. 1 (figures of the ratio not shown).

4. Space-time structures of the ISOs

The space-time structure of the ISO can be understood with the help of phase composites. The amplitude $A(t)$ and phase $\phi(t)$ of the ISO, as a function of time t, are determined by following the method suggested by Moron *et al*. (1998). The space-time evolution of the ISO during an averaged cycle of the oscillation, with ϕ varying from 0 to 2π, is described by constructing the phase composites of the RC. Considering eight phase intervals, such that $(k-1)\pi/4 \le \phi \le k\pi/4$ where $k = 1, 2, \ldots, 8$, the RC is averaged over all ϕ in each phase interval k over the entire time length of the RC to obtain the phase composites.

4.1. Boreal summer MISO

The phase composites of the precipitation RC of the boreal summer MISO for phase intervals 1 through 4 are shown in Figs. 4a and 4b, respectively, for observation and May forecasts. In the case of the model, the phase composite is the average of all the ensemble members. The phase composites cover May–September of all years. In phase 1 of the phase composite of the observation (Fig. 4a), positive anomalies of precipitation are present over a

large area from the Arabian Sea to the West Pacific in a tilted pattern while negative anomalies are present to north over the foothills of the Himalayas and the West Pacific. A weak band of negative anomalies extends along the ITCZ up to the west coast of North America in the Pacific. The band of positive anomalies moves northward in phases 2 and 3, resulting in the establishment of the active phase over India. At the same time, negative anomalies appear in the equatorial Indian Ocean in phase 2 and expand and propagate eastward in phase 3 while the negative anomalies from the previous cycle grow along the west coast of North America. In phase 4, the negative anomalies further expand and move northward over the Indian peninsula and the Bay of Bengal and the positive anomalies move further northeastward over the Pacific. Since the phase composites are averages over many cycles of MISO, the composites in phases 5–8 (figure not shown) are almost mirror images of phases 1–4, respectively, with anomalies of opposite sign. During phases 6–7, the break phase is established over India.

The phase composites of the MISO simulated by the model's May forecasts (Fig. 4b) show good correspondence with the composites of observation (Fig. 4a) in spatial structure, magnitude and propagation. The tilted structure of the positive anomalies, which results from northward propagation starting at different times because of eastward propagation along the equatorial region, is well simulated by the model in both the spatial extent and the magnitude. The genesis of the negative anomalies and the subsequent expansion and propagation in the Indian Ocean are also captured by the model. The model forecasts also show northward propagation in the West Pacific. Yet, there are some differences between the model and observation. The band of anomalies along the Pacific ITCZ is very weak although the model is able to generate the signal along the west coast of North America. The anomalies in the forecasts are weaker over India and do not propagate as north as they do in the observation. This is

consistent with the model's deficit in the standard deviation over India (Fig. 3g). The leading ISO in CFSv1, which had a longer period at 106 days, exhibited northward and eastward propagation over the Indian region but not over the Maritime Continent and West Pacific (Achuthavarier and Krishnamurthy 2011a). The magnitude of this ISO was considerably less over most of the region. Another ISO in CFSv1, with a period of 57 days, showed poor propagation properties over the entire region. The MISO in CFSv2 seems to simulate the spatial structure, magnitude and propagation better than the ISOs in CFSv1.

The eastward and northward propagations are important features of MISO, which can be further examined through Hovmöller diagrams. For this purpose, the phase composites of MISO RC were constructed at phase intervals of length *À*/12. The eastward propagation mainly takes place over the equatorial region. Therefore, the phase composite of the RC, averaged over 10°S–10°N, is shown as longitude-phase diagram in Figs. 5a and 5b, respectively, for observation and May forecasts. In the observation, there is an eastward propagation to the east of 60°E (Fig. 5a). This eastward propagation is clearly seen in the phase composites of the forecasts also (Fig. 5b) but does not extend as far east as in the observation. The forecast anomalies are weaker over the Maritime Continent and the West Pacific. The northward propagation over the monsoon region is determined by averaging the MISO RC over 60°E–95°E and plotting it as latitude-phase diagram, as shown in Figs. 5c and 5d, respectively, for observation and forecasts. The observation shows southward propagation to the south of the equator and northward propagation to the north of the equator (Fig. 5c). The model also shows northward propagation from the equator but ends at 21°N which is about 2–3° short of observation (Fig. 5d). The southward propagation to the south of the equator is not as pronounced as in the observation.

4.2. Boreal winter MJO

The phase composites of the precipitation RC for the first half cycle of the boreal winter MJO for are shown in Figs. 6a and 6b for observation and November forecasts, respectively. The phase composite in the model is the average of all the ensemble members. The phase composites cover the period of November–March each year. In the observation (Fig. 6a), strong negative anomalies are present around a part of the Maritime Continent and the northern coast of Australia along with weak positive anomalies in the Indian Ocean and Central Pacific in phase 1. The negative anomalies move eastward into the SPCZ, forming a tilted pattern during phases 2–4. The positive anomalies intensify and also propagate eastward in the region south of the equator from phase 2 to 4. At the same time, a thin band of positive anomalies appear along the ITCZ in the Pacific, slightly north of the equator. However, there is no signal at the coast of North America as in the case of MISO during the boreal summer.

In the model's November forecasts, the phase composites of the MJO (Fig. 6b) reproduce the spatial structure, magnitude and propagation of the observed composites (Fig. 6a) fairly well. The eastward propagation of the negative anomalies from the Maritime Continent to the central Pacific is also simulated by the model, including the tilted structure in the SPCZ. The magnitude of these anomalies is slightly higher compared to observation, consistent with the model's excess standard deviation over the Pacific (Fig. 3h). Positive anomalies are generated in the Indian Ocean in phase 1 and expand in phase 2 but with lesser magnitude. In phases 3–4, the positive anomalies move eastward but with slightly higher magnitude compared to observation. However, the positive anomalies also expand westward in the Indian Ocean, unlike in the observation. The model shows the observed thin band of positive anomalies in the ITCZ over the Pacific. The assessment of CFSv1 by Pegion and Kirtman (2008b) showed that the boreal winter MJO

simulated by CFSv1 had less spatial extent compared to observation and was not well organized over the Indian Ocean. The period of the MJO was also much longer, similar to MISO, in CFSv1 with slower propagation and stalling over the Maritime Continent. The space-time structure of the winter MJO in CFSv2 seems to show improved spatial coverage and propagation properties.

The propagation properties of the MJO in both the observation and model forecasts can be further studied with Hovmöller diagrams using the RCs constructed at phase interval of length $\grave{A}/12$. The longitude-phase cross-section of the RC averaged over 10°S–10°N reveals clear eastward propagation in observation (Fig. 7a) and November forecasts (Fig. 7b). The latitude-phase cross-section of the MJO RC, averaged over 90°E–120°E, suggests southward propagation to the south of the equator in observation (Fig. 7c) but not in the model forecasts (Fig. 7d). However, there is northward propagation of weaker anomalies between equator and 10°N in both observation and model. The lack of strong southward propagation to the south of the equator in the MJO is a big difference with the MISO which showed strong northward propagation.

4.3. Simulation of phases

The phase composites of the model forecasts, discussed previously, have fairly good correspondence with the observed composites. The composites were computed on the basis of phase intervals varying from 0 to $2\grave{A}$ for each oscillation. Here, the phases of the model ISOs are compared with those of the observation in actual time. The EIMR index of the MISO RC from observation and May forecasts is plotted in Figs. 8a for the period May–September 2001, as an example. The nonlinear oscillatory behavior is clearly evident in both observation and forecasts. Although the amplitude of the model's MISO is comparable to that of the observation, the phase varies with considerable difference among the ensemble members of the forecast and between

forecast and observation. While some of the ensemble members of the forecasts stay somewhat closer to the observation for some time, others differ considerably from the beginning of the forecast period. All the forecasts are out of phase by about the middle of July.

The model forecast seems to be better when the initial amplitude and initial phase of the model ISO are closer to those of the ISO in observation (Fig. 8b). Two forecasts starting on 6 May (6 hours apart) stay close to the observed MISO until the middle of July, implying a considerably high predictability. The two forecasts, while staying close to each other, diverge from the observation and become out of phase by the middle of August. Two other forecasts, initiated on 16 May (6 hours apart), are out of phase with the observation right from the beginning and throughout the entire period. The two forecasts, however, stay close to each other.

Similar behavior is also seen in the MJO during the boreal winter. The MAMR index of the MJO is shown in Fig. 8c for observation and November forecasts for the period Nov 2001 – March 2002. The amplitude of the forecast MJO is comparable to that of the observation. In this case also, the phase of the forecast MJO displays considerable variability among the ensemble members. Several ensemble members of the forecast stay closer to the observation until the beginning of January. Almost all the forecasts are out of phase beyond the middle of January. In the winter MJO forecasts (Fig. 8c), more ensemble members seem to evolve closer to the observation for about two months compared to the summer MISO forecasts (Fig. 8a).

4.4. Relation with circulation

The features of circulation associated with MISO and MJO are now studied. Some possible mechanisms involving circulation for the propagation of the ISOs are also examined. In both the boreal summer and winter ISOs, there is a strong coupling between the zonal circulation

and convection. The relation of the precipitation ISOs with the circulation is examined with the help of phase composites of zonal wind using the CFSR data for observation and model forecasts. The phase composites of 850 hPa zonal wind anomalies for the first half cycle of the boreal summer MISO are shown in Figs. 9a and 9b for observation and May forecasts, respectively. The wind composites were constructed using the same phases as in the precipitation composites (section 4.1). The period covers May–September each year, and total anomalies of the zonal wind are used. Positive anomalies appear in the equatorial India Ocean in phase 1, and then strengthen, expand in zonal direction and move northward into the Indian subcontinent during phases 2–4 in the observation (Fig. 9a). Negative anomalies accompany to the north and south of the positive anomalies. These correspond to the anti-cyclonic flow over India and cyclonic flow in the Indian Ocean. The northward propagation of the zonal wind is consistent with the precipitation composites (Fig. 4a) and with the MISO of circulation discussed by Krishnamurthy and Achuthavarier (2012). The Pacific is mostly covered by easterlies except for westerlies near the west coast of North America and South America in phase 1. The spatial structure, magnitude and the northward propagation of MISO in the model forecasts (Fig. 9b) have good correspondence with the observation (Fig. 9a) in all the four phase intervals. However, the zonal wind is considerably weaker over most of the central and eastern Pacific.

The phase composites of 850 hPa zonal wind for the boreal winter MJO are presented in Figs. 10a and 10b for observation and November forecasts, respectively. The period covered is November–March of each year. In the observation (Fig. 10a), easterlies propagate from the equatorial Indian Ocean to the Pacific Ocean during phases 1–4, followed by westerlies in the Indian Ocean. Corresponding to the precipitation zones (Fig. 6a), the westerlies and easterlies are present to the west and east of the positive anomalies of precipitation, respectively, in each

phase. This is consistent with the known evolution of the convection-circulation coupling (e.g., Sperber 2003; Zhang 2005). The composites of the model forecasts (Fig. 10b) also reveal easterlies propagating eastward, followed by westerlies, along the equatorial Indian and Pacific Oceans during phases 1–4, similar to the evolution in observation (Fig. 10a). The westerlies are weaker in phase 2 while the easterlies are weaker over the northern part of the Pacific in the model compared to observation.

To show that convectively coupled process is involved in the model's ISOs, the phase composites of the outgoing longwave radiation (OLR), which represents deep convection, are constructed. The phase composites of OLR for the first half cycle of MISO (boreal summer) and MJO (boreal winter) in the model forecasts are plotted in Figs. 11a and 11b, respectively. The amplitude, structure and propagation of the OLR have good correspondence with those of precipitation in both MISO (Figs. 11a and 4b) and MJO (Figs. 11b and 6b). The coupling between convection and circulation is revealed when compared with the composites of low-level zonal wind (Figs. 9b and 10b). In MISO, the anti-cyclonic (cyclonic) flow (Fig. 9b) is accompanied by enhanced (suppressed) convection (Fig. 11a). The eastward propagating convection zones in MJO (Fig. 11b) are accompanied by westerlies to the west and easterlies to the east (Fig. 10b). Thus, the model forecasts capture the observed convectively coupled circulation during summer and winter.

A simple mechanism for the meridional propagation of convection involves low-level cyclonic vorticity and moisture convergence to the north of the convection zone (e.g., Goswami, 2005). To examine this mechanism and to find further relation with circulation, the phase composites of 850 hPa relative vorticity and 200 hPa divergence are studied through Hovmöller diagrams. The longitude-phase cross section of 850 hPa vorticity averaged over 10°S–10°N in

MISO is shown in Figs. 12a and 12b for observation and May forecasts, respectively. The corresponding composites of the precipitation RC are also shown. The positive (negative) vorticity is ahead to the east of the precipitation (dry) zones during the eastward propagation both in the observation and model forecasts. However, the vorticity is weaker in the model and does not extend as far east as in the observation. The latitude-phase cross-sections of 850 hPa vorticity and the precipitation RC averaged over 60°E–95°E are plotted in Figs. 12c and 12d for observation and forecasts, respectively. In the observation (Fig. 12c), the precipitation (dry) zone is led by cyclonic (anticyclonic) vorticity to the north of the equator during the northward propagation. A similar phase relation between vorticity and precipitation is evident in the forecasts also (Fig. 12d). A consistent phase relation between vorticity and precipitation is also seen to the south of the equator in both observation and forecasts.

The phase composites of 200 hPa divergence and the corresponding precipitation RC are shown in Fig. 13 for MISO. The longitude-phase cross section averaged over 10°S–10°N (Fig. 13a) in observation shows that precipitation (dry) regions are co-located with the upper level divergence (convergence), indicating deep convection process. Similar relation between the upper level divergence and precipitation is also evident in the May forecasts (Fig. 13b), although with less intensity. The divergence in the model does not extend as far eastward as in the observation. The latitude-phase cross sections averaged over 60°E–95°E show more intense divergence (convergence) at upper level co-located with the precipitation (dry) zone and propagating north both in observation (Fig. 13c) and May forecasts (Fig. 13d).

For the MJO during DJFM, the longitude-phase cross section of the phase composites of 850 hPa relative vorticity and the precipitation RC averaged over 10°S–10°N are plotted in Figs. 14a and 14b for observation and November forecasts, respectively. In the observation, positive

(negative) vorticity leads the precipitation with pronounced eastward propagation (Fig. 14a). This phase relation between vorticity and precipitation is well captured by the forecasts (Fig. 14b). The latitude-phase cross section averaged over 90°E–120°E of vorticity shows weaker southward propagation to the south of the equator in the observation (Fig. 14c). The precipitation (dry) zone is led by cyclonic (anticyclonic) vorticity. The model forecasts also reproduce the weak southward propagation and the observed phase relation with the precipitation (Fig. 14d).

The phase composites of 200 hPa divergence and the precipitation RC for the MJO are shown in Fig. 15. The divergence and precipitation are co-located in MJO also and show strong eastward propagation in the longitude-phase cross section averaged over 10°S–10°N in the observation (Fig. 15a). The November forecasts also reveal the in-phase relation between divergence and precipitation along with eastward propagation (Fig. 15b). The latitude-phase cross-section averaged over 90°E–120°E also shows the in-phase relation between divergence and precipitation both in observation (Fig. 15c) and forecasts (Fig. 15d). However, the divergence does not reveal even weaker southward propagation.

5. Summary and discussion

In the tropical regions, the prediction of climate variability at intraseasonal time scale is important because of the impact of ISOs and challenging because of the complexity of the problem. Predictions beyond the weather time scale and up to a season are now part of operational forecasting centers. The NCEP has been carrying out seasonal predictions since 2004 using CFSv1 and by its successor CFSv2 since 2011. The present study has analyzed the simulation of the tropical ISOs by CFSv2 during boreal summer and winter. The retrospective forecasts prepared by the NCEP for the period 1982–2010 were examined to determine the

model's ability to simulate the summer MISO and winter MJO. Comparison with the observations and the ISOs simulated by CFSv1 was also carried out. The CFSv2 was found to simulate the spatial structure, period and propagation of MISO and MJO with reasonably good correspondence with the observation and showed improvement over CFSv1.

The leading ISOs were extracted from the daily precipitation anomalies of the ensemble of forecasts and observation by using MSSA. This data-adaptive method did not require any pre-assumption on the time scale of the extracted eigenmodes. The ensemble members of the forecasts are able to exhibit nonlinear oscillations which emerged as leading ISOs. The May forecasts of the model simulate the spatial structure and evolution of the summer MISO with good resemblance to the observation. The model's MISO also reproduces observed northward and eastward propagation over the Indo-Pacific region. The model falls slightly short in its northward propagation over India. The variance of MISO is comparable to observation over most of Indo-Pacific region except for deficit over India and the Maritime Continent. The peak period of the MISO in the model's ensemble members ranges from 47 to 70 days with an average period of 61 days which is higher than the observed period of 45 days. This discrepancy is also reflected through the ensemble spread in the phase of the MISO compared to observation. The model also showed the observed relation with the lower level zonal wind in spatial structure and propagation except for weaker magnitude over the Pacific. The model also revealed the coupling between circulation and convection in MISO. The observed phase relations of precipitation with low-level relative vorticity and upper-level divergence involved in the zonal and meridional propagations were reproduced by the forecasts.

The boreal winter MJO in the November forecasts of the model is also reasonably well simulated in comparison to observation. The peak period of the ensemble members of the

forecast is in the range 60–72 days with an average period of 67 days, higher than the observed period of 54 days. Although the spatial structure of the variance of the forecast MJO is similar to the observation, the variance is higher in the model over the SPCZ and less over the Maritime Continent. The simulation of the space-time evolution of the winter MJO by the model forecasts is comparable to the observation. The model reproduces the eastward propagation of the MJO signal with appropriate magnitude and spatial structure. However, the anomalies are more extended over the Indian Ocean. The westerlies and easterlies relative to the precipitation zone are also well simulated by the model in the lower level although with lesser magnitude over certain parts of the Pacific. The convectively coupled circulation was also evident in the model's MJO. The observed phase relation between precipitation and low-level vorticity and between precipitation and upper-level divergence were also captured by the model.

There is no discernable difference in the model's ability to simulate the boreal summer MISO and winter MJO. Although many features of the ISOs are reasonably well simulated by the model, there is a considerable ensemble spread in the phase of the model ISOs compared to observation. However, if the initial phase and the amplitude of the model ISO are closer to those of the observed ISO, the forecast ISO evolves close to the observed ISO for about two months, showing higher predictability. Compared with the CFSv1 simulations analyzed by earlier studies (Pegion and Kirtman 2008a, 2009b; Achuthavarier and Krishnamurthy 2011a, 2011b), CFSv2 seems to have improved the simulation of both summer MISO and winter MJO in period, spatial structure and propagation. The reasons for the improvement in CFSv2 need further investigation. The earlier studies on CFSv1 pointed out the important role of air-sea interaction, especially over the Indian Ocean, in both the ISOs. It is of interest to determine if the air-sea interaction and heat budget are better over the Indian Ocean in CFSv2. Mechanistic experiments with regional

decoupling separately over the Indian and Pacific Oceans using CFSv2 will be helpful.

Acknowledgments

This work was supported by National Science Foundation (grant ATM-0830068), National Oceanic and Atmospheric Administration (grant NA09OAR4310058), and National Aeronautics and Space Administration (grant NNX09AN50G). The author thanks NCEP for reforecasts of CFSv2.

References

Achuthavarier D, Krishnamurthy V. 2011a. Daily modes of South Asian summer monsoon variability in the NCEP Climate Forecast System. *Clim. Dyn.* **36**: 1941–1958.

Achuthavarier D, Krishnamurthy V. 2011b. Role of Indian and Pacific SST in Indian summer monsoon intraseasonal variability. *J. Clim.* **24**: 2915–2930.

Allen MR, Robertson AW. 1996. Distinguishing modulated oscillations from coloured noise in multivariate datasets. *Clim. Dyn.* **12**: 775–784.

Allen MR, Smith LA. 1996. Monte Carlo SSA: Detecting irregular oscillations in the presence of colored noise. *J. Clim.* **9**: 3373–3404.

Annamalai H, Slingo HM. 2001. Active/break cycles: diagnosis of the intraseasonal variability of the Asian summer monsoon. *Clim. Dyn.* **18**: 85–102.

Annamalai H, Sperber KR. 2005. Regional heat sources and the active and break phases of boreal summer intraseasonal (30-50 day) variability. *J. Atmos. Sci.* **62**: 2726–2748.

Broomhead DS, King GP. 1986. Extracting qualitative dynamics from experimental data. *Physica D* **20**: 217–236.

Fu X, Wang B, Li T, McCreary JP. 2003. Coupling between northward-propagating, intreaseasonal oscillations and sea surface temperature in the Indian Ocean. *J. Atmos. Sci.* **60**: 1733–1753.

Ghil M, Allen MR, Dettinger MD, Ide K, Kondrashov D, Mann ME, Robertson AW, Saunders A, Tian Y, Varadi F, Yiou P. 2002. Advanced spectral methods for climatic time series. *Rev. Geophys.* **40(1)**: 1003, doi:10.1029/2000RG000092.

Goswami BN. 2005. South Asian monsoon. In *Intraseasonal variability in the atmosphere-ocean climate system*, Lau WKM, Waliser DE (eds). Praxis: Chichester, 19–61.

Goswami BN, Krishnamurthy V, Annamalai H. 1999. A broad-scale circulation index for the interannual variability of the Indian summer monsoon. *Q. J. R. Meteorol. Soc.* **125**: 611–633.

Hazra A, Krishnamurthy V. 2015. Space-time structure of diabatic heating in monsoon intraseasonal oscillation. *J. Clim.* **28**: 2234-2255.

Huffman GJ, Adler RF, Bolvin DT, Gu G, Nelkin EJ, Bowman KP, Hong Y, Stocker EF, Wolff DB. 2007. The TRMM Multisatellite Precipitation Analysis (TMPA): Quasi-global, multi-year, combined-sensor precipitation estimates at fine scales. *J. Hydrometeorol.* **8**: 38–55.

Hung M-P, Lin J-L, Wang W, Kim D, Shinoda T, Weaver SJ. 2013. MJO and convectively coupled equatorial waves simulated by CMIP5 climate models. *J. Clim.* **26**: 6185–6214.

Kang I-S, Jin K, Wang B, Lau K-M, Shukla J, Krishnamurthy V, Schubert SD, Waliser DE, Stern WF, Kitoh A, Meehl GA, Kanamitsu M, Galin VY, Satyan V, Park C-K, Liu Y. 2002. Intercomparison of the climatological variations of Asian summer monsoon precipitation simulated by 10 GCMs. *Clim. Dyn.* **19**: 383–395.

Kim D, Sperber K, Stern W, Waliser D, Kang I-S, Maloney E, Wang W, Weickmann K, Benedict J, Khairoutdinov M, Lee M-I, Neale R, Suarez M, Thayer-Calder K, Zhang G. 2009. Application of MJO simulation diagnostics to climate models. *J. Clim.* **22**: 6413–6436.

Klingaman NP, Woolnough SJ. 2014. The role of air-sea coupling in the simulation of the Madden-Julian oscillation in the Hadley Centre model. *Q. J. R. Meteorol. Soc.* **140**: 2272–2286.

Krishnamurthy V, Achuthavarier D. 2012. Intraseasonal oscillations of the monsoon circulation over South Asia. *Clim. Dyn.* **38**: 2335–2353.

Krishnamurthy V, Kinter JL III. 2003. The Indian monsoon and its relation to global climate variability. In *Global climate*, Rodó X, Comín FA (eds). Springer: Berlin, 186–236.

Krishnamurthy V, Shukla J. 2000. Intraseasonal and interannual variability of rainfall over India. *J. Clim.* **13**: 4366–4377.

Krishnamurthy V, Shukla J. 2007. Intraseasonal and seasonally persisting patterns of Indian monsoon rainfall. *J. Clim*. **20**: 3–20.

Krishnamurthy V, Shukla J. 2008. Seasonal persistence and propagation of intraseasonal patterns over the Indian monsoon region. *Clim. Dyn.* **30**: 353–369.

Lau K-M, Chan PH. 1986. Aspects of the 40–50 day oscillation during the northern summer as inferred from outgoing longwave radiation. *Mon. Wea. Rev.* **114**: 1354–1367.

Lin J-L, Kiladis GN, Mapes BE, Weickmann KM, Sperber KR, Lin W, Wheeler MC, Schubert SD, Del Genio A, Donner LJ, Emori S, Gueremy J-F, Hourdin F, Rasch P, Roeckner E, Scinocca JF. 2006. Tropical intraseasonal variability in 14 IPCC AR4 climate models. Part I: Convective signals. *J. Clim.* **19**: 2665–2690.

Madden RA, Julian PR. 1971. Description of a 40–50 day oscillation in the zonal wind in the tropical Pacific. *J. Atmos. Sci.* **28**: 702–708.

Madden RA, Julian PR. 1972. Description of global-scale circulation cells in the tropics with a 40–50 day period. *J. Atmos. Sci.* **29**: 1109–1123.

Madden RA, Julian PR. 1994. Observations of the 40-50 day tropical oscillation – A review. *Mon. Wea. Rev.* **122**: 814–837.

Moron V, Vautard R, Ghil M. 1998. Trends, interdecadal and interannual oscillations in global

sea-surface temperatures. *Clim. Dyn.* **14**: 545–569.

Pegion K, Kirtman BP. 2008a. The impact of air-sea interactions on the predictability of the tropical intraseasonal oscillation. *J. Clim.* **21**: 5870–5886.

Pegion K, Kirtman BP. 2008b. The impact of air-sea interactions on the simulation of tropical intraseasonal variability. *J. Clim.* **21**: 6616–6635.

Plaut G, Vautard R. 1994. Spells of low-frequency oscillations and weather regimes in the Northern Hemisphere. *J. Atmos. Sci.* **51**:210–236.

Saha S, Nadiga S, Thiaw C, Wang J, Wang W, Zhang Q, Van den Dool HM, Pan H-L, Moorthi S, Behringer D, Stokes D, Peña M, Lord S, White G, Ebisuzaki W, Peng P, Xie P. 2006. The NCEP Climate Forecast System. *J. Clim.* **19**: 3483–3517.

Saha S, Moorthi S, Pan H-L, Wu X, Wang J, Nadiga S, Tripp P, Kistler R, Woollen J, Behringer D, Liu H, Stokes D, Grumbine R, Gayno G, Wang J, Hou Y-T, Chuang H-Y, Juang H-MH, Sela J, Iredell M, Treadon R, Kleist D, Van Delst P, Keyser D, Derber J, Ek M, Meng J, Wei H, Yang R, Lord S, Van den Dool H, Kumar A, Wang W, Long C, Chelliah M, Xue Y, Huang B, Schemm J-K, Ebisuzaki W, Lin R, Xie P, Chen M, Zhou S, Higgins W, Zou C-Z, Liu Q, Chen Y, Han Y, Cucurull L, Reynolds RW, Rutledge G, Goldberg M. 2010. The NCEP Climate Forecast System Reanalysis. *Bull. Amer. Meteorol. Soc.* **91**: 1015–1057.

Saha S, Moorthi S, Wu X, Wang J, Nadiga S, Tripp P, Behringer D, Hou Y-T, Chuang H-Y, Iredell M, Ek M, Meng J, Yang R, Mendez MP, Van den Dool H, Zhang Q, Wang W, Chen M, Becker E. 2014. The NCEP Climate Forecast System Version 2. *J. Clim.* **27**: 2185–2208.

Sikka DR, Gadgil S. 1980. On the maximum cloud zone and the ITCZ over Indian longitudes during the southwest monsoon. *Mon. Wea. Rev.* **108**: 1840–1853.

Sperber KR. 2003. Propagation and the vertical structure of the Madden-Julian Oscillation. *Mon. Wea. Rev.* **131**: 3018–3037.

Sperber KR, Annamalai H. 2008. Coupled model simulations of boreal summer intraseasonal (30-50 day) variability, Part I: Systematic errors and caution on use of metrics. *Clim. Dyn.* **31**: 345–372.

Sperber KR, Annamalai H, Kang I-S, Kitoh A, Moise A, Turner A, Wang B, Zhou T. 2013. The Asian summer monsoon: an intercomparison of CMIP5 vs. CMIP3 simulations of the late 20th century. *Clim. Dyn.* **41**: 2711–2744.

Waliser DE, Jin K, Kang I-S, Stern WF, Schubert SD, Wu MLC, Lau K-M, Lee M-I, Krishnamurthy V, Kitoh A, Meehl GA, Galin VY, Satyan V, Mandke SK, Wu G, Liu Y, Park C-K. 2003. AGCM simulations of intraseasonal variability associated with the Asian summer monsoon. *Clim. Dyn.* **21**: 423–446.

Wang B, Ding Q, Fu X, Kang I-S, Jin K, Shukla J, Doblas-Reyes F. 2005. Fundamental challenge in simulation and prediction of summer monsoon rainfall, *Geophys. Res. Lett.* **32**: L15711. doi:10.1029/2005GL022734.

Wang W, Hung M-P, Weaver SJ, Kumar A, Fu X. 2014. MJO prediction in the NCEP Climate Forecast System version 2. *Clim. Dyn.* **42**: 2509–2520.

Yasunari T. 1979. Cloudiness fluctuations associated with the northern hemisphere summer monsoon. *J. Meteorol. Soc. Japan* **57**: 227–242.

Zhang C. 2005. Madden-Julian Oscillation. *Rev. Geophys.* **43**: RG2003. doi:10.1029/2004RG000158.

Figure captions

Fig. 1. JJAS seasonal climatological mean of precipitation in (a) observation (TRMM) and (b) May forecasts of the model (CFSv2), and standard deviation of daily mean precipitation during JJAS season in (d) observation and (e) May forecasts of the model. DJFM seasonal climatological mean of precipitation in (f) observation (TRMM) and (g) November forecasts of the model and standard deviation of daily mean precipitation during DJFM season in (i) observation and (j) November forecasts of the model. Difference in climatological mean between model and observation for (c) JJAS and (h) DJFM seasons. Units are in mm day^{-1}.

Fig. 2. Active composite minus break composite of daily precipitation anomalies during JJAS season in (a) observation (TRMM) and (b) model's May forecasts. The active and break periods used in the composites are based on the EIMR index of observation in (a) and EIMR index of model forecasts in (b). The EIMR index is the average of precipitation anomaly over the domain (70°E–100°E, 10°N–30°N) shown as green box in (a). The model composite based on EIMR index in observation (TRMM) is shown in (c). The active and break periods used in (c) are same as those used in (a). Active composite minus break composite of daily precipitation anomalies during DJFM season in (d) observation (TRMM) and (e) model's November forecasts. The active and break periods used in the composites are based on the MAMR index of observation in (d) and MAMR index of model forecasts in (e). The MAMR index is the average of precipitation anomaly over the domain (110°E–150°E, 20°S–0°) shown as green box in (d). The model composite based on MAMR index in observation (TRMM) is shown in (f). The active and break periods used in (f) are same as those used in (d). The model composites are averages of all the ensemble members. Units are in mm day^{-1}.

Fig. 3. Power spectra of ISO in TRMM observation (red) and in the ensemble members

of the model forecasts (blue) for (a) boreal summer and (b) boreal winter. The model forecasts are from May initial conditions in (a) and from November initial conditions in (b). Standard deviation of daily RC of MISO in (c) observation and (e) May forecasts of the model, and (g) difference in the standard deviation between the model and observation for boreal summer. Standard deviation of daily RC of MJO in (d) observation and (f) November forecasts of the model and (h) difference in the standard deviation between the model and observation for boreal winter. Units are in mm day^{-1}.

Fig. 4. Phase composites of precipitation RC for four phase intervals of ISO cycle in (a) TRMM observation and (b) model forecasts for boreal summer. The phase number is given at the top right corner of each panel. The model forecasts are from May initial conditions. The phase composites are averages of composites of all the ensemble members of the forecasts. Units are in mm day^{-1}.

Fig. 5. Longitude-phase cross-section of the phase composites of the RC of MISO averaged over 10°S–10°N in (a) observation and (c) model forecasts, and latitude-phase cross-section of the phase composites of the RC of MISO averaged over 65°E–95°E in (b) observation and (d) model forecasts for boreal summer. The model forecasts are from May initial conditions. Units are in mm day^{-1}.

Fig. 6. Phase composites of precipitation RC for four phase intervals of ISO cycle in (a) TRMM observation and (b) model forecasts for boreal winter. The phase number is given at the top right corner of each panel. The model forecasts are from November initial conditions. The phase composites are averages of composites of all the ensemble members of the forecasts. Units are in mm day^{-1}.

Fig. 7. Longitude-phase cross-section of the phase composites of the RC of MJO

averaged over 10°S–10°N in (a) observation and (c) model forecasts, and latitude-phase cross-section of the phase composites of the RC of MJO averaged over 90°E–120°E in (b) observation and (d) model forecasts for boreal winter. The model forecasts are from November initial conditions. Units are in mm day^{-1}.

Fig. 8. (a) EIMR index of the RC of MISO in TRMM observation (red) and individual ensemble members of the model forecasts from May initial conditions (blue) for 2001. (b) Same as (a) but shown for forecasts from initial conditions of 6 May and 16 May only. (c) MAMR index of the RC of MJO in TRMM observation (red) and individual ensemble members of the model forecasts from November initial conditions (blue) for 2001–2002.

Fig. 9. Phase composites of total anomalies of zonal wind at 850 hPa for four phase intervals of MISO cycle in (a) TRMM observation and (b) model forecasts for boreal summer. The phase number is given at the top right corner of each panel. The model forecasts are from May initial conditions. The phase composites are averages of composites of all the ensemble members of the forecasts. Units are in m s^{-1}.

Fig. 10. Phase composites of total anomalies of zonal wind at 850 hPa for four phase intervals of MJO cycle in (a) TRMM observation and (b) model forecasts for boreal winter. The phase number is given at the top right corner of each panel. The model forecasts are from November initial conditions. The phase composites are averages of composites of all the ensemble members of the forecasts. Units are in m s^{-1}.

Fig. 11. Phase composites of total anomalies of OLR for four phase intervals of (a) the MISO cycle during the boreal summer and (b) the MJO cycle during boreal winter in the model forecasts. The phase number is given at the top right corner of each panel. The model forecasts are from (a) May and (b) November initial conditions. The phase composites are averages of

composites of all the ensemble members of the forecasts. Units are in W m^{-2}.

Fig. 12. Longitude-phase cross-section (shaded) of the phase composites of total anomalies of vorticity at 850 hPa averaged over 10°S–10°N in (a) observation and (b) model forecasts, and latitude-phase cross-section (shaded) of the phase composites of total anomalies of vorticity at 850 hPa averaged over 65°E–95°E in (c) observation and (d) model forecasts for boreal summer. The model forecasts are from May initial conditions. The unit of vorticity is 10^{-6} s^{-1}.The corresponding cross-sections of the precipitation RC of MISO are also plotted as contours at an interval of 0.8 mm day^{-1}. Positive (negative) values are plotted as solid (dashed) contours.

Fig. 13. Longitude-phase cross-section (shaded) of the phase composites of total anomalies of divergence at 200 hPa averaged over 10°S–10°N in (a) observation and (b) model forecasts, and latitude-phase cross-section (shaded) of the phase composites of total anomalies of divergence at 200 hPa averaged over 65°E–95°E in (c) observation and (d) model forecasts for boreal summer. The model forecasts are from May initial conditions. The unit of divergence is 10^{-6} s^{-1}.The corresponding cross-sections of the precipitation RC of MISO are also plotted as contours at an interval of 0.8 mm day^{-1}. Positive (negative) values are plotted as solid (dashed) contours.

Fig. 14. Longitude-phase cross-section (shaded) of the phase composites of total anomalies of vorticity at 850 hPa averaged over 10°S–10°N in (a) observation and (b) model forecasts, and latitude-phase cross-section (shaded) of the phase composites of total anomalies of vorticity at 850 hPa averaged over 90°E–120°E in (c) observation and (d) model forecasts for boreal winter. The model forecasts are from November initial conditions. The unit of vorticity is 10^{-6} s^{-1}.The corresponding cross-sections of the precipitation RC of MJO are also plotted as

contours at an interval of 0.8 mm day^{-1}. Positive (negative) values are plotted as solid (dashed) contours.

Fig. 15. Longitude-phase cross-section (shaded) of the phase composites of total anomalies of divergence at 200 hPa averaged over 10°S–10°N in (a) observation and (b) model forecasts, and latitude-phase cross-section (shaded) of the phase composites of total anomalies of divergence at 200 hPa averaged over 90°E–120°E in (c) observation and (d) model forecasts for boreal winter. The model forecasts are from November initial conditions. The unit of divergence is 10^{-6} s^{-1}.The corresponding cross-sections of the precipitation RC of MJO are also plotted as contours at an interval of 0.8 mm day^{-1}. Positive (negative) values are plotted as solid (dashed) contours.